

1 Mitochondrial dysfunction drives a neuronal exhaustion phenotype 2 in methylmalonic aciduria 3

4 **Matthew C.S. Denley¹, Monique S. Straub¹, Giulio Marcionelli¹, Miriam A. Güra¹, David
5 Penton², Igor Delvendahl³, Martin Poms⁴, Beata Vekeriotaitė⁵, Sarah Cherkoui⁶,
6 Federica Conte⁷, Ferdinand von Meyenn⁵, D. Sean Froese¹✉, Matthias R.
7 Baumgartner¹**

8 ¹Division of Metabolism and Children's Research Center, University Children's Hospital
9 Zurich, University of Zurich, Zurich, Switzerland CH-8032.

10 ²Electrophysiology Core Facility, University of Zurich, Zurich, Switzerland CH-8057.

11 ³ Department of Molecular Life Sciences, University of Zurich, Zurich, Switzerland CH-8057.

12 ⁴ Clinical Chemistry and Biochemistry and Children's Research Center, University Children's
13 Hospital Zurich, University of Zurich, Zurich, Switzerland CH-8032.

14 ⁵ Laboratory of Nutrition and Metabolic Epigenetics, Institute for Food, Nutrition and Health,
15 Department of Health Sciences and Technology, ETH Zurich, Zurich, Switzerland CH-8603.

16 ⁶ Pediatric Cancer Metabolism Laboratory, Children's Research Center, University Children's
17 Hospital Zurich, University of Zurich, Zurich, Switzerland CH-8032.

18 ⁷ Department of Neurology, Donders Institute for Brain, Cognition and Behavior, Radboud
19 University Medical Center, 6525 GA Nijmegen, Netherlands.

20 ✉e-mail correspondance to: Sean.Froese@kispi.uzh.ch;
21 Matthias.Baumgartner@kispi.uzh.ch

24 **Abstract**

25 **Methylmalonic aciduria (MMA) is an inborn error of metabolism resulting in loss of
26 function of the enzyme methylmalonyl-CoA mutase (MMUT). Despite acute and
27 persistent neurological symptoms, the pathogenesis of MMA in the central nervous
28 system is poorly understood, which has contributed to a dearth of effective brain
29 specific treatments. Here we utilised patient-derived induced pluripotent stem cells
30 and *in vitro* differentiation to generate a human neuronal model of MMA. We reveal
31 strong evidence of mitochondrial dysfunction caused by deficiency of MMUT in
32 patient neurons. By employing patch-clamp electrophysiology, targeted
33 metabolomics, and bulk transcriptomics, we expose an altered state of excitability,
34 which is exacerbated by application of 2-dimethyloxoglutarate, and we suggest may
35 be connected to metabolic rewiring. Our work provides first evidence of
36 mitochondrial driven neuronal dysfunction in MMA, which through our
37 comprehensive characterisation of this paradigmatic model, enables first steps to
38 identifying effective therapies.**

39 **Introduction**

40 Mitochondrial diseases are a diverse group of genetic disorders that lead to dysfunctional
41 mitochondria and energetic depletion. Pathogenic variants in approximately 1136 genes
42 which encode mitochondrial-resident proteins¹, found on both nuclear and mitochondrial
43 DNA, may cause mitochondrial diseases. Together, 23 per 100,000 people harbour
44 pathogenic variants that have or will convey a mitochondrial disease². However, the inherent
45 clinical and genetic heterogeneity of mitochondrial diseases make them difficult to diagnose,
46 hard to treat, and complex to study^{3,4}. Nevertheless, mitochondrial diseases affecting
47 components of oxidative phosphorylation (OXPHOS) or proteins proximal to the tricarboxylic
48 acid cycle (TCA cycle) often report overlapping symptoms^{5,6}, particularly within the central
49 nervous system (CNS)^{7,8}.

50 Isolated methylmalonic aciduria (MMA) is an archetypical mitochondrial disease
51 caused by pathogenic variants leading to the absence or deficiency of the nuclear-encoded
52 mitochondrial matrix-residing enzyme methylmalonyl-CoA mutase (MMUT; MIM #251000)⁹.
53 It is typified by accumulation of methylmalonic acid and related compounds in blood and

55 urine; however, increased levels of these disease-related compounds are likely not sufficient
56 to explain overall clinical presentation and disease progression^{10,11}. Rather, reduced
57 mitochondrial function and energy production may also be important contributors to disease
58 progression^{10,12-15}. Mitochondrial structural changes and dysfunction have been widely
59 described in MMA^{12,16,17}. Previous liver and kidney tissue models have demonstrated MMUT-
60 deficiency causes enlarged mitochondria and altered OXPHOS activity^{16,17}. The
61 consequences of this appear to be impaired mitophagy¹² and shifted anaplerosis into the
62 TCA cycle^{10,18}. MMUT-KO cells and MMA patient fibroblasts have demonstrated a
63 preference for reductive TCA cycle pathway, which was rescued by supplying cells with 2-
64 dimethyloxoglutarate, an analogue of 2-oxoglutarate¹⁰. However, neither mitochondrial nor
65 metabolic response to MMUT-deficiency in the CNS have been investigated due to the lack
66 of an adequate model.

67 In the CNS, glutamine and glutamate have tissue-specific functions as stimulatory
68 neuroactive molecules¹⁹. Additionally, mitochondria preferentially utilise OXPHOS for
69 synaptic transmission and maintaining membrane potential through Na/K-ATPases²⁰⁻²³.
70 Despite the clear role of neurological dysfunction in MMA and the long-term symptoms (i.e.,
71 metabolic stroke, epilepsy, optic neuropathy) invoked, no appropriate models have been
72 employed to investigate this aspect of the disease. Such a shortfall is important because
73 current treatments of MMA are symptomatic and do not protect against long-term CNS
74 sequelae. Recent advances of patient-derived induced pluripotent stem cell (iPSC)-models
75 offer an invaluable route to model neuronal dysfunction in MMA and provide valuable
76 insights into CNS dysfunction.

77 In this study, we generated iPSC-derived neuronal models of MMA from variant-
78 matched patient fibroblasts. We demonstrate that MMUT-deficient neurons have perturbed
79 mitochondrial networks and reduced mitochondrial function. These appear to drive action
80 potential attenuation in patient-derived neurons, potentially through reduced sodium
81 currents. To tie metabolism to cellular function, metabolomic and transcriptomic exploration
82 suggest altered glutamine processing, which is exacerbated by application of 2-
83 dimethyloxoglutarate. Altogether, our results demonstrate that mitochondrial dysfunction
84 may lead to a neuronal exhaustion-like phenotype, which may be an important component of
85 neurological dysfunction in MMA.

86

87 **Results**

88 **Generation of MMUT-deficient iPSC-derived neuronal lines**

89 Deficiency of MMUT causes MMA, leading to biochemical alterations which drive disease
90 pathology (Fig. 1a). Using Sendai virus based OKSM (OCT4, KLF4, SOX2, MYC)
91 reprogramming, we generated iPSC clones from two unrelated individuals, each
92 homozygous for the pathogenic, vitamin B₁₂/cobalamin-unresponsive^{24,25} variant MMUT-
93 p.(Asn219Tyr) (Pt1 & Pt2, *n* = 2; decimals indicate subclone, e.g. Pt1.1 is patient 1, subclone
94 1), and a wildtype control individual (Ct1, *n* = 1) (Fig. 1b and Supp. Fig. 1a). Isolated clones
95 from all three iPSC lines did not retain Sendai virus markers used in ectopic pluripotency
96 induction (Supp. Fig. 1b). These cell lines were characterised alongside a commercially
97 available control (Ct2, *n* = 1). All four iPSC lines expressed the endogenous pluripotency
98 markers: KLF-4, SOX2, OCT4 and NANOG, which were not found in the progenitor
99 fibroblasts, except for KLF-4 which is natively expressed in fibroblasts (Supp. Fig. 1c). We
100 demonstrated expression of the pluripotency markers NANOG and SSEA-4, and pan-stem
101 cell marker SOX2, as well as the proliferative marker Ki67 (Fig. 1b), and could generate the
102 three germ layers in all four cell lines (Fig. 1c). Comparative genomic hybridization indicated
103 that induction of pluripotency did not generate *de novo* copy number variations between
104 fibroblasts and their daughter iPSC clones (Supp. Fig. 2).

105 To evaluate whether the generated iPSC clones demonstrated MMUT deficiency, we
106 examined MMUT protein expression by immunocytochemistry (Fig. 1d) and Western blotting
107 analysis (Fig. 1e). Using a MMUT specific antibody (Supp. Fig. 1d and 1e), we observe a

108 more punctate and less intense staining pattern, which does not co-localise well with
109 translocase of the outer mitochondrial membrane complex subunit 20 (TOMM20) (Fig. 1d)
110 and we found reduced MMUT protein in lysates of patient iPSCs (Fig. 1e), consistent with
111 reduced enzymatic activity (2.58% of control), as demonstrated by an indirect activity assay
112 which monitors propionate incorporation via MMUT into the TCA cycle²⁶ (Fig. 1f).

113
114 To assess if MMUT deficiency affects neuronal development and function, we employed a
115 2D differentiation protocol that utilises dual-SMAD inhibition to generate dorsal forebrain-
116 enriched neuronal progenitors^{27,28} (Fig. 2a). For all control and patient-derived iPSCs, we
117 identified successful generation of neuroectodermal Nestin- and SOX2-positive
118 neuroepithelium which progressively differentiated from a population including SOX2- and
119 PAX6-positive neural stem cells (NSC) to TUBB3 and EOMES-positive neural progenitor
120 cells and finally TUBB3, TBR1, MAP2, and NeuN-positive neurons (Fig. 2b). RT-qPCR
121 revealed that patient cells express SOX2, PAX6, and EOMES at days 13 and 21 *in vitro*
122 comparably to control cells when expression is normalized to day 0 (Fig. 2c). This suggests
123 they adopt cortical NSC identity at the same rate as control cell lines. Immunocytochemistry
124 (Fig. 2d) and Western blotting analysis (Fig. 2e) indicate MMUT protein expression is
125 retained in NSC and neurons (Fig. 2d), however patient-derived neurons maintain the more
126 punctate and less intense MMUT staining pattern and show reduced MMUT protein levels
127 (Fig. 2e).

128
129 **Patient neurons have mitochondrial dysfunction and disrupted networks**

130 TOMM20 is an essential mitochondrial protein often used as a proxy for mitochondrial
131 abundance and shape²⁹. Immunocytochemistry demonstrated altered TOMM20 staining
132 patterns in patient-derived neurons that can be described as perinuclear and smaller (Supp.
133 Fig. 3a), suggestive of disrupted mitochondrial networks. This was consistently observed in
134 neurons derived from both patient lines, but not controls and was related to the extent to
135 which MMUT could be detected within individual neurons (Fig. 3a and Supp. Fig. 3b).
136 Investigation of spatial mitochondrial characteristics of patient neurons using TOMM20
137 staining revealed reduced mitochondrial volume and diameter but not sphericity (Supp. Fig.
138 3c,d). Further, disrupted mitochondrial networks in patient neurons appeared to impair
139 mitochondrial response to OXPHOS insult, as demonstrated by comparable MitoSOX
140 fluorescence at baseline but significantly reduced intensity after treatment with complex I
141 inhibitor rotenone (Supp. Fig. 3e). In patient-derived cells, we identified two apparent
142 populations, those expressing detectable MMUT (MMUT+) which overlapped with TOMM20,
143 and those without (MMUT-) (Fig. 3a,b). To investigate the functional capacity of patient
144 MMUT+ and MMUT- mitochondria, we used detectable fluorescence of
145 tetramethylrhodamine-methyl-ester (TMRM) as a measure of mitochondrial membrane
146 potential. We found a reduced TMRM signal in patient-derived neurons, a difference that
147 was exacerbated in those cells with no detectable MMUT (Fig. 3c,d). We hypothesized that
148 the lower TMRM signal denoted lower electron transport chain function, which we tested by
149 inhibiting complex I with rotenone. We found reduced TMRM fluorescence in rotenone
150 treated MMUT+ cells, less so in patient MMUT-, but not in control (Fig. 3d), suggesting that
151 MMUT deficient mitochondria have a diminished proton motive force leaving them less able
152 to react to events that would dissipate the membrane potential. We hypothesized that
153 reduced membrane potential could trigger programmed cell death. Strikingly, this was
154 supported by untreated patient-derived neurons having increased proportion of pro-apoptotic
155 cleaved Caspase 3 (Fig. 3e) as well as DAPI nuclei staining patterns consistent with
156 apoptotic cells (Fig. 3f and Supp. Fig. 3f).

157
158 **Electrophysiological assessment reveals an exhaustion phenotype in patient-derived**
neurons

159 In order to assess generated neurons' functional properties, we performed whole-cell
160 analysis on patient ($n = 132$, Pt1 & Pt2) and control ($n = 94$, Ct1 & Ct2) neurons (Supp. Tab.
161 1). Similar to previous reports³⁰, principle component analysis (PCA) of all 31 extracted

162 features from step current injection protocols (Supp. Tab. 2) revealed three distinct clusters
163 (Supp. Fig. 4a), which were further discriminated by utilizing 21 primary variables (Fig. 4a
164 and Supp. Fig. 4b). These clusters could be best represented as non-action potential (AP)
165 firing (Type 1, T1), single-AP firing (T2), and multiple AP-firing (T3) neurons (Fig. 4a,b and
166 Supp. Fig. 4a). They were not separated by genotype (patient vs control) (Supp. Fig. 4b), but
167 rather by variation within inherent electrophysiological properties, such as resting membrane
168 potential, input resistance, capacitance, number of APs, and AP threshold (Supp. Fig. 4c).
169 Unguided hierarchical clustering of 21 primary variables separated assessed neurons by T1,
170 T2 or T3, but not by genotype (Supp. Fig. 4d). However, we observed an apparent decrease
171 in T3 and corresponding increase in T2 in patient-derived neurons (Fig. 4c), suggesting that
172 generating successive APs may be corrupted in patient neurons.

173 To explore this further, we performed correlation analysis on 21 primary variables in
174 T3 neurons derived from patients ($n = 50$) and controls ($n = 52$) (Fig. 4d). For all cells, we
175 identified anticipated correlations between variables, such as AP threshold and AP full width
176 at half maximum (FWHM, i.e. time between slope rise and fall at half-max amplitude) with
177 AP amplitude (negative correlations), as well as AP amplitude with AP number and resting
178 membrane potential with AP FWHM (positive correlations) (Fig. 4d and Supp. Fig. 5a,b).
179 Striking, however, was that variables expected to correlate with AP attenuation, and found to
180 do so in control neurons (e.g., AP amplitude, AP threshold, and FWHM), did not correlate in
181 patient neurons (Fig. 4d and Supp. Fig. 5c). Closer inspection of the reduction of AP
182 amplitude following multiple APs (measured as the attenuation ratio), revealed a significantly
183 stronger loss of AP amplitude and hence enhanced attenuation in patient neurons (Fig. 4e).
184 This is indicative of a mitochondrial exhaustion-like phenotype, which is mirrored in Leigh
185 Syndrome models that lacked repetitive spiking and contained higher numbers of non-
186 spiking neurons³¹.

187 To link the loss of AP amplitude over multiple firings and mitochondrial dysfunction,
188 we further assessed attenuation in selected cells whose mitochondrial morphology was
189 visualized using MitoTracker™ (Supp. Fig. 5d). Consistent with previous data (Supp. Fig.
190 3a-d), all control cells appeared to have intact mitochondrial networks, whereas patient-
191 derived cells had either intact or disrupted mitochondrial networks (Supp. Fig. 5d). Patient
192 cells with intact mitochondrial networks had an attenuation ratio similar to control neurons,
193 whereas neurons with disrupted mitochondrial networks had increased attenuation (Supp.
194 Fig. 5e), suggesting an association between AP exhaustion and mitochondrial dysfunction.

195 Depolarisations generating higher AP amplitudes are achieved by influxes of cations;
196 the velocity of these influxes can be calculated through the first derivative of the membrane
197 potential slope over time (dVdt, Fig. 4f). dVdt ratios in patient-derived neurons were
198 decreased compared to controls (Supp. Fig. 5f), which was driven by the depolarisation
199 (reported as maximum) and not repolarisation (potassium efflux, reported as minimum)
200 phase (Fig. 4g). In control neurons, the maximum dVdt positively correlated with the
201 attenuation ratio, a relationship which was lost in patient-derived neurons (Supp. Fig. 5g).
202 Similarly, the positive correlation of dVdt with AP number and with AP amplitude found in
203 control neurons was lost or reduced in patient-derived cells (Fig. 4d and Supp. Fig. 5h).
204 These findings suggest that patient-derived cells cannot sustain sufficient current densities
205 to maintain action potential firing, which may lead to the observed exhaustion-like
206 phenotype.

207 To test the hypothesis that reduced sodium currents drive these observations, we
208 performed additional voltage-clamp recordings on patient ($n = 92$) and control ($n = 89$)
209 neurons. The selected neurons contained the same patient T3 proportional decrease (Supp.
210 Fig. 6a), increased attenuation and decreased dVdt ratio as the overall population (Supp.
211 Fig. 6b). We found substantially reduced sodium current densities in patient-derived neurons
212 when compared to control, with peak densities reduced 5-fold in patient-derived neurons
213 (Fig. 4i,j; Supp. Fig. 6c-e).

214 215 **Rewired glutamine-glutamate metabolism alters glutamatergic identity**

216 We next utilised targeted metabolomics to investigate the connection between
217 mitochondrial dysfunction and altered neuronal excitability. MMA related metabolites,

218 including hydroxypropionic acid and propionyl-carnitine were elevated as expected in
219 patient-derived neurons, while lactate tended to be increased with methylmalonic acid and 2-
220 methylcitrate appearing unchanged (Fig. 5a and Supp. Fig. 7a). Despite our finding of
221 disturbed mitochondrial networks in patient-derived neurons, we found no difference in the
222 pools of the anaplerotic intermediates pyruvate, alanine, glutamine and glutamate (Supp.
223 Fig. 7b) as well as TCA cycle intermediates (Supp. Fig. 7c) between patient and control-
224 derived neurons, which is consistent with findings in patient fibroblasts¹⁰. This prompted us
225 to investigate the anaplerotic contribution to the TCA cycle from labelled glutamine (Fig. 5b).
226 Glutamine flows into the TCA cycle via glutamate and 2-oxoglutarate (Fig. 5b). Following
227 labelled glutamine supplementation, we found a high proportion of labelled glutamine, which
228 was reduced in glutamate and 2-oxoglutarate, but found no difference between fractional
229 labelling (Supp. Fig. 7d) nor pool levels (Supp. Fig. 7e) of all three intermediates between
230 patient and control-derived neurons. We also found no difference in the fractional
231 incorporation nor pool levels of measured TCA intermediates (Supp. Fig. 7f,g). However, we
232 did notice reduced fractional incorporation, but not pool levels, of aspartate (Fig. 5c).
233 Glutamine-derived aspartate can be produced via oxaloacetate by cytosolic or mitochondrial
234 aminotransferases, whereby the direction of the TCA cycle (oxidative or reductive)
235 influences the number of labelled carbons (Fig. 5b). We found the ratio of M+5 to M+4
236 citrate, and M+3 to M+4 malate (M+x refers to the number of carbon isotopes that are
237 present, where a ratio of 1 indicates equal contribution from oxidative and reductive), to be
238 changed in patient-derived neurons (Fig. 5d). This altered ratio is supportive of metabolic
239 rewiring in the sense that labelled carbons entering the TCA cycle are affected in patient-
240 derived cells, which is also supported by altered aspartate labelling.

241 We also investigated the pool sizes of glycolytic intermediates, which follows report
242 of increased hexoses in primary patient fibroblasts¹⁰. Using a targeted approach to measure
243 levels of specific detectable sugar phosphates³², we identified elevated galactose-1-
244 phosphate, mannose-6-phosphate, and glucosamine-6-phosphate in patient-derived
245 neurons compared to controls (Supp. Fig. 8a). We found reduced *N*-acetyl-glucosamine-6-
246 phosphate and *N*-acetyl-mannosamine-6-phosphate (Supp. Fig. 8b) and elevated nucleotide
247 sugars GDP-fucose and GDP-mannose (Supp. Fig. 8c). We suspect this may be indicative
248 of a reactive shift to glycolysis, as OXPHOS in disease contexts is impaired, which is a
249 phenomena also described in hypoxia³³. We found no change in other glucose or fructose
250 phosphate derivatives nor pentose phosphate derivatives (Supp. Fig. 8a,d and Supp. Tab. 3).
251 Our finding of elevated galactose-1-phosphate and mannose-6-phosphate suggest glycolytic
252 flux is increased. Further investigation is required to determine a link between increased
253 glycolytic metabolites and rewired TCA cycle metabolism, as this phenomena has been
254 reported previously¹⁰.

255 Based on the above changes, we attempted to rescue the phenotype in patient-
256 derived neurons using dimethyl-2-oxoglutarate (DM-2OG) a membrane permeable analogue
257 of the TCA cycle intermediate 2-oxoglutarate (Fig. 5e). Application of DM-2OG increased
258 some but not all pools of TCA cycle intermediates measured, including glutamate and
259 glutamine (Supp. Fig. 9a-b), and resulted in amelioration of the difference between pool
260 levels of hydroxypropionic acid, propionyl-carnitine, and lactate (Fig. 5f, Supp. Fig. 9c) as
261 well as fractional contribution into aspartate of control and patient-derived neurons and
262 normalisation of TCA cycle flux (Fig. 5g-i). DM-2OG supplementation increased selected
263 hexose phosphates but patient galactose-1-phosphate, mannose-6-phosphate, and
264 glucosamine-6-phosphate remained significantly increased compared to treated control
265 neurons (Supp. Fig. 9d). However, DM-2OG treatment reduced the difference between
266 patient and control *N*-acetyl-glucosamine-6-phosphate and *N*-acetyl-mannosamine-6-
267 phosphate (Supp. Fig. 9e), which we attribute to DM-2OG flooding the TCA cycle and
268 conversion of glutamine to glucosamine that then inhibits side pathways³⁴.

269 **270 TCA cycle rewiring impacts neuronal excitability at the synaptic level**

271 DM-2OG altered the neuronal levels of neurotransmitter amines, such as glutamate, leading
272 us to investigate the effect of DM-2OG supplementation and subsequent metabolic rewiring
273 on electrophysiological properties. We performed current-clamp recordings on 36 neurons
274 with supplementation of DM-2OG between 0.1 – 6.0 mM (Supp. Fig. 10a). We found that
275 higher doses abolished AP firing capacity (Supp. Fig. 10a), which may be linked to
276 increasing hyperpolarisation and decreasing capacitance (Supp. Fig. 10b-c). Voltage-clamp
277 recordings on control neurons demonstrated that 1 mM and 6 mM DM-2OG reduced sodium
278 current densities to levels that were similar to untreated patient-derived neurons (Fig. 6a,b).
279 At lower doses, control but not patient-derived neurons were still able to produce APs and
280 maintain sodium current densities (Fig. 6a-b and Supp. Fig. 10a). We hypothesized that
281 patient metabolic rewiring altered neuronal function at the synaptic level. We investigated
282 the packaging of glutamate in the synapse through *SLC17A7*, which encodes the vesicular
283 glutamate transporter 1 (VGLUT1). We found a greater number of VGLUT1+ foci in patient
284 neurons (Supp. Fig. 10d,e), suggesting a predisposition towards glutamate excitotoxicity that
285 could contribute to the exhaustion phenotype, and, more generally, to the neurological
286 phenotype. Consequently, we recorded spontaneous excitatory postsynaptic currents of
287 untreated patient ($n = 46$) and control ($n = 48$) as well as 0.1mM DM-2OG treated patient (n
288 = 7) and control ($n = 8$) neuronal networks. We observed an increased charge of synaptic
289 events in patient-derived neurons (Fig. 6c,d). However, we did not observe difference in
290 event amplitude, decay kinetics, or frequency (Supp. Fig. 10f-h). The event duration (charge)
291 may be related to glutamate receptor subunits, which combine to form functional neuronal
292 glutamate receptors³⁵.

293 Given the electrophysiological and metabolic changes in patient-derived neurons, we
294 performed bulk transcriptomics on control and patient neurons. Analysis of the neuronal
295 transcriptome via PCA revealed successful separation of controls and patients based on
296 inherent variance (Supp. Fig. 11a). Using over-representation analysis, we found gene
297 networks involved in “glutamatergic synapse”, “ion channel activity”, and “chemical synaptic
298 transmission” to be differentially expressed (Fig. 6e and Supp. Fig. 11b-c). Further analysis
299 revealed glutamate packaging machinery (*SLC17A7*), and glutamate receptors, such as
300 *GRM7*, *GRIN3A*, *GRIA3*, *GRIA4*, to have altered expression in patient-derived neurons (Fig.
301 6f and Supp. Fig. 11d). We also observed several ion channel genes, including sodium
302 (*SCN9A*), calcium (*CACNA1H*), and potassium (*KCNH3*, *KCNN1*, *KCNIP3*) channels, to be
303 differentially expressed (Fig. 6f). Moreover, *GAD1/2*, which catalyses the production of 4-
304 aminobutanoate (GABA) from glutamate, depending on the supply pool size of glutamate in
305 the cytosol, appeared to be downregulated in patient-derived neurons (Fig. 6f).

306 To test if subunit composition is altered, we treated control and patient neurons with
307 0.1 mM DM-2OG and analysed the transcriptome. Comparison of untreated control and DM-
308 2OG supplemented patient-derived neurons revealed the absence of many previously
309 identified significantly differentially regulated synaptic related GO terms (Fig. 6g). Of
310 previously identified glutamatergic synapse differentially expressed genes, only *GRM7*,
311 *GRIN3A*, *SCN9A*, *KCNN1*, and *GRIA3* were still significant (Fig. 6h). Disease-state
312 metabolic rewiring changes the TCA cycle, an impact that we can replicate with DM-2OG
313 treatment. We demonstrate DM-2OG increases metabolite pools, such as glutamate, and
314 these treatments recapitulate aspects of the exhaustion phenotype.

315 Finally, we leveraged our bulk transcriptomic data to perform RNA-seq deconvolution
316 protocols to achieve pseudo single-cell RNA-seq data for cell type. This analysis revealed
317 that the largest cellular population across all cell lines were those with excitatory neuron
318 cellular identity (Supp. Fig. 11e), although each population was heterogenous and also
319 contained inhibitory neurons and astroglia precursors, in line with the findings of the original
320 methods paper²⁷. We were also able to extract specific gene transcripts that identify specific
321 cellular populations such as region-specific proliferating cells (PCNA, DCX, PAX3, PAX6,
322 HES6), discrete neuronal populations (*SLC17A6*, *GAD2*), and astrocytic precursor
323 populations (*GJA1*, *ADGRV1*) (Supp. Fig. 11f). DM-2OG was not found to have any
324 consistent effect on cell type across the various lines (Supp. Fig. 11e). As patient liver
325 biopsy had found reduced protein expression of cytochrome c oxidase (COX)³⁶, we report
326 mitochondrial COX transcripts (MT-CO1, MT-CO2, MT-CO3) are not differentially

327 expressed, conversely subunits COX5A and COX6B were upregulated in patient-derived
328 neurons (Supp. Fig. 11g).

329
330 **Discussion**

331 In this study, we have gained insight into the conserved role of mitochondrial disruption in
332 MMA and uncovered an exhaustion-like phenotype in neurons affected by mitochondrial
333 disease. We described how mitochondrial disruption and reduced sodium current density
334 underlie AP attenuation. MMUT deficiency rewires neuronal metabolism and conferred a
335 greater demand of glutamine and aspartate to the TCA cycle, we also documented reduced
336 current density through modulation of synaptic ion channel dynamics. We introduce the first
337 *in vitro* human-relevant neurological model of MMA. We were able to model one common
338 European pathogenic variant c.655A>T. However, we were unable to generate an isogenic
339 control due to the genomic landscape of the mutation site. A further caveat is the use of only
340 two control lines, and a lack of neural cell-type characterization using single cell RNA-seq.
341 However, since we observed comparable rates of cortical marker adoption and gross
342 electrophysiological functionality of patient-derived cells were indistinguishable from control
343 neurons, we expect that the excitatory populations generated across conditions were
344 comparable. Nevertheless, we make the final note that experiments making use of
345 MitoTracker and TMRM were not performed with an additional cell-type specific marker, and
346 we therefore cannot determine exactly which cell-types are most prone to mitochondrial
347 dysfunction.

348 The occurrence of neurological symptoms despite treatment highlights the need to
349 explore neuronal pathomechanisms³⁷⁻⁴³. Our findings reinforce previous comprehensive
350 evidence that mitochondrial dysfunction drives pathophysiology in MMA^{12,16,17}. These
351 evidence fit well within the current literature that describe reduced mitochondrial respiration
352 and/or mitochondrial ultrastructure alterations in primary patient kidney cells¹²; liver, kidney,
353 heart, and skeletal muscle of patients¹³; Mut^{-/-} mice kidney¹⁷ and liver¹⁶. Here we
354 demonstrate that mitochondrial dysfunction is also an important component of neuronal
355 pathology. Although electrophysiology has never been assessed in MMA, two separate
356 iPSC-derived models of the primary mitochondrial disease Leigh Syndrome demonstrate
357 that pathogenic variants in the electron transport chain reduced oxygen consumption^{31,44}.
358 Electrophysiological reporting was mixed, one study found SURF1 mutations reduced
359 sodium and potassium currents, which resulted in reduced repetitive spiking³¹. Another
360 paper concluded that no difference between patient and control cells' intrinsic properties
361 were found⁴⁴.

362 Although the term "attenuation" is not used in these referenced papers, it is clear that
363 reduced sodium currents and decreased AP amplitudes are present³¹ and current-evoked
364 AP amplitudes decrease over time. This phenomenon is demonstrated more clearly in a
365 current ramp test, however both examples demonstrate an exhaustive phenotype
366 comparable to attenuation⁴⁴. These findings can be related back to biophysical studies in
367 sodium inactivation which posit that complex gating can be tied to the specific subpopulation
368 of sodium channel by the incorporation of specific subunits⁴⁵. This consideration is even
369 more striking when we consider our findings of differential regulation of a number of sodium
370 channel subunits.

371 Neurons have been shown to have a greater reliance on OXPHOS during AP
372 firing^{46,47}. One route to meeting such a demand in the brain is through the oxidation of
373 glutamine⁴⁸⁻⁵¹, which is coupled to incremental glucose oxidation⁵¹. Derangement of
374 OXPHOS puts a greater reliance on glutamine and aspartate metabolism⁵². Our finding of
375 reduced glutamine contribution to aspartate suggests rewiring of the TCA flux⁵³, consistent
376 with reduced reliance on reductive TCA cycle flux in patient-derived neurons. This pattern is
377 consistent with a greater importance on anaplerotic metabolites. Elevated levels of lactate
378 and hexose phosphate sugars suggest glucose flowing into glycolysis may also be rewired
379 to side pathways⁵⁴. Altered dependence of patient neurons on glutamine and aspartate may
380 feasibly lead to differential expression of glutamatergic receptor subunits. Hippocampal
381 neurons rapidly redistribute their glutamate receptors after glutamate and glycine
382 treatment^{55,56}, indicating that metabolic shift may be strong enough to cause the differential

383 expression of ionotropic glutamate receptors observed in patient neurons. Concurrently this
384 may result in patient neurons' prolonged synaptic events or reduced ability to sustain
385 successive action potentials. *GRIA4*, which is downregulated in patient cells, is the fastest
386 glutamate receptor and its expression is linked to receptor kinetics⁵⁷. *GRIA4*-containing
387 AMPA receptors also appear responsive to changes in spontaneous synaptic events⁵⁸.

388 Previous work in our laboratory found disease-specific biochemical alterations in
389 patient fibroblasts¹⁰. Crucially, our findings mirror the results from patient fibroblasts in a
390 reduced propionate incorporation, elevated propionyl-carnitine and hydroxy-propionate,
391 although we did not identify increased methylmalonic acid nor 2-methylcitrate. Manipulation
392 of disease-state metabolic rewiring with DM-2OG demonstrated a rescue of disease-related
393 metabolites but exacerbated components of the exhaustion phenotype in control-derived
394 neurons. This suggests an association between metabolic rewiring and gene expression.
395 Decreased measurements of *N*-acetyl-glucosamine-6-phosphate and *N*-acetyl-
396 mannosamine-6-phosphate may link changes in the hexosamine biosynthesis pathway to
397 altered transcription, as this pathway contributes posttranslational modifications to
398 intracellular proteins, including glycosylation and associated transcription factors.
399 Furthermore, the use of DM-2OG and its effect on glutamate, a neurotransmitter, evidenced
400 these effects by abolition of AP firing capacity.

401 To date, great focus has been placed on the basal ganglia, due to the occurrence of
402 bilateral lesions within the basal ganglia, we chose to focus our efforts on cortical neurons.
403 The reasoning behind this decision was three-fold: (1) protocols to generate glutamatergic
404 neurons of the cortical forebrain are better characterised and more sophisticated than
405 GABAergic neurons or cholinergic interneurons of the telencephalon. (2) In individuals
406 affected by MMA, bilateral lacunar infarctions of the basal ganglia are often reported after
407 acute metabolic decompensation, which produces movement disorder, however other
408 neurological symptoms such as delayed myelination, subcortical white matter changes,
409 cortical atrophy, and brain stem and cerebellar changes are also commonly reported. From
410 this list of symptoms, multiple cell types are affected, however no information has been
411 published concerning which cellular populations generate these symptoms mechanistically.
412 Moreover, whilst we and others have shown that MMUT is expressed in neurons⁵⁹, it has yet
413 to be demonstrated to be expressed in astroglia, microglia, or oligodendrocytes, and yet is
414 believed to be a ubiquitously expressed key enzyme in cellular metabolism. This raises the
415 question of how MMUT is regulated at the protein level, which may account for our
416 observation of the two populations, MMUT+ and MMUT-. It has been shown that MMA leads
417 to aberrant post-translational modifications by methymalonylation⁶⁰. Moreover, novel
418 phosphorylation sites in MMUT have been identified in liver samples⁶¹. Future work could
419 look to identify the phosphoproteome during mitochondrial insult to identify a regulatory
420 framework that leads to MMUT mislocalisation. (3) In acute excitotoxicity, the primary line of
421 investigation centres around the idea that excessive postsynaptic depolarisation leads to
422 cellular death, which may cause lesions seen in MMA but also in diseases such as
423 Parkinson's. However, we have no indication to believe that dopaminergic signalling is the
424 reason behind basal ganglia lesions in MMA. Hence, excessive glutamate in the synapse
425 from pre-synaptic cortical neurons innervating the striatum is just as likely a cause of
426 excitotoxic cellular death and possibly cortical atrophy.

427 Here, we describe a mechanism of mitochondrial disruption generating reduced AP
428 firing in patient-derived cells affected by MMA. Underlying this AP exhaustion was a reduced
429 sodium current density, rewired glutamine metabolism, and differential glutamate receptor
430 transcript expression. Further manipulation of glutamine metabolism reverses some of the
431 metabolic and transcriptomic observations. More work will be required to elucidate the exact
432 mechanism that reduces excitability in patient neurons.

434 **Methods**

435 **Ethics statement, patients and fibroblast lines**

436 Approval to use patient fibroblasts was granted by the Cantonal Ethics Commission of
437 Zurich (KEK-ZH-Nr. 2014-0211, amendment PB_2020-00053). Both patient-derived
438 fibroblast lines carried the *MMUT* homozygous pathogenic variant c.655A>T (p.Asn219Tyr),

439 confirmed by Sanger sequencing at the DNA level, and corresponding to the mut⁰
440 phenotype. In addition to fibroblasts from two affected individuals (Pt1, female; Pt2, male),
441 fibroblasts from Ct1 (ATCC: CRL-2522, male) were used for iPSC generation. An additional
442 iPSC line control (Ct2, male; NHLBli003-A, RRID: CVCL_1E78) was acquired from Rutgers
443 University (RUCDR, USA) ⁶².
444

445 **Fibroblast and HEK293T culture, and maintenance**

446 HEK293T (ATCC: CRL-3216) and fibroblasts were cultured at 37°C and 5% CO₂ in a
447 humidified incubator. Cells were cultured in Dulbecco's modified eagle medium (DMEM,
448 Gibco, Cat. 31966-047) supplemented with 10% foetal bovine serum (FBS, Gibco, Cat.
449 102070-106) and 1% Anti-Anti (100X, Antibiotic-Antimycotic, Gibco, Cat. 15240-062).
450 Passaging was performed once cells reached 80% confluence, using 0.05% Trypsin (1X,
451 Trypsin-EDTA, Gibco, Cat. 25300-054) and washed with Dulbecco's Phosphate Buffered
452 Saline (DPBS, Gibco, Cat. 14190-250). Cells were maintained frozen in liquid nitrogen in
453 cryopreservation medium (90% FBS (as before) and 10% DMSO (Sigma, Cat. D2438-
454 50ML)).
455

456 **iPSC culture, differentiation, and maintenance**

457 All cells were cultured at 37°C and 5% CO₂ in a humidified incubator. The generation of
458 iPSCs from fibroblasts was performed as previously described⁶³. Briefly, the transduction
459 was performed using the CytoTune®-iPS 2.0 Sendai Reprogramming Kit (Invitrogen, Cat.
460 A16518) according to the manufacturer's instructions. Transduction was performed on
461 fibroblasts with passage numbers lower than five. Cells were plated at a density of 1x10⁵
462 cells/well in a 12-well plate. Non-integrating Sendai virus was added to the fibroblast
463 medium at an MOI (ratio virus to cells) of 5 for KOS (Klf4, Oct4, Sox2) and c-Myc, and MOI 3
464 for Klf4. 8000 transduced fibroblasts were plated on inactivated mouse embryonic fibroblasts
465 (MEFs). Derived iPSCs colonies were transferred to feeder-free conditions using 1mg/mL
466 Collagenase type IV solution (Gibco, Cat. 17104019).

467 Feeder-free iPSC colonies were maintained as previously described⁶⁴ with minor
468 modifications. Between culturing, cells were maintained frozen in liquid nitrogen in
469 cryopreservation medium (90% KnockOut™ Serum Replacement, Gibco, Cat. 10828028;
470 10% DMSO, Sigma, Cat. D2438). Cells were cultured on 0.17 mg/well (6-well) or 0.083
471 mg/well (12-well) BME matrix (Cultrex® Reduced Growth Factor Basement Membrane
472 Extract, PathClear®, Cat. 3433-010-01) in Essential 8 medium (Gibco, Cat. A1517001)
473 supplemented with 100 U/mL Penicillin-Streptomycin (10'000 U/mL, Gibco, Cat. 15140122).
474 Passaging was performed once colonies reached 80% confluence using EZ-LiFT Stem Cell
475 Passaging Reagent per manufactures instructions (Sigma-Aldrich, SCM139) after which 10
476 µL/mL RevitaCell™ Supplement (100X, Gibco, Cat. A2644501) was applied to passaged
477 iPSC colonies. For neural induction, single cell passaging of iPSCs was performed using 0.5
478 mL or 1 mL ACCUTASE™ Cell detachment solution (1X, StemCellTechnologies, Cat.
479 07920) for 12-well and 6-well plates, respectively, and 2 µL/mL from 5 mM ROCK-inhibitor
480 Y-27632 (Dihydrochloride; Sigma-Aldrich, Cat. SCM075) was applied for single cell
481 passaging. Cells were inspected daily using the Leica DMIL microscope and bright-field
482 culturing images were taken using the Leica Application Suite (LAS) Version 2.8.1 software.
483

484 **Array comparative genomic hybridization**

485 To test the genetic integrity of fibroblast-derived iPSCs pre- and post-induction, DNA
486 extracts from fibroblasts and iPSCs were assessed using array comparative genomic hybrid
487 analysis (Cell Guidance Systems). Briefly, DNA was isolated from cell pellets using DNeasy
488 Blood & Tissue Kit (Qiagen, Cat. 69504) per manufacturer's instructions. All extracted DNA
489 had a concentration >50 ng/µL and contained more than 1 µg. Purity was measured using an
490 ND-1000 Spectrophotometer (NanoDrop Technologies, Inc.) and fell within A260/A230 = 1.8
491 – 2.2 and A260/A280 > 1.8. The array contained 754,027 distinct probes and analysis was
492 conducted on the Infinium Global Screening Array v3.0 platform. The genome-wide
493 resolution was ~200 kb. Copy number variations and loss of heterozygosity was reported in
494 samples when present in at least ~15 – 20% of cells. The report can be found in
Supplementary Figure 2.

495 **Germ-layer differentiation assay**

496 iPSCs were differentiated to the three germ layers as previously described^{65,66} with minor
497 modifications. Cells were plated onto a 12-well plate in chemically defined medium with
498 polyvinyl alcohol (CDM-PVA: 250 mL IMDM, LifeTechnologies Cat. 21980032); 250 mL
499 DMEM/F-12 + GlutaMAX (Gibco, Cat. 31765027); 1 mL Concentrated Lipids (Life
500 Technologies, Cat. 11905031); 20 μ L 1-Thioglycerol (Sigma, Cat. M6145-25ML); 350 μ L
501 Insulin (Sigma, Cat. I9278-5ML); 250 μ L Transferrin (Sigma, Cat. 10652202001); 10 mL
502 PVA (10 g [stock: 0.05 g/mL], (Sigma, Cat. P8136-250G) in 200 mL embryo-grade water
503 (Sigma, Cat. W1503)). For one day CDM-PVA was supplemented with 10 ng/mL Activin
504 (Gibco, PHC9564) and 12 ng/mL fibroblast growth factor-2 (FGF2) (Gibco, Cat. PHG0024).
505 Thereafter, lineage specific protocols were followed, as reported below.

506 For endoderm, 100 ng/mL Activin, 80 ng/mL FGF2, 10 ng/mL BMP-4 (Gibco,
507 PHC9534), 10 μ M LY294002 (Gibco, Cat. PHZ1144), and 3 μ M CHIR99021 (Sigma, Cat.
508 SML1046-5MG) were supplemented in CDM-PVA medium for one day. The next day, the
509 medium was refreshed at the same concentrations without CHIR99021. On the third day, the
510 medium was changed to RPMI medium (500 mL RPMI1640 + GlutaMAX (LifeTechnologies,
511 Cat. 61870010); 10 mL B27 (Gibco, Cat. 17504044); 5 mL NEAA (Gibco, Cat. 11140035); 5
512 mL Pen/Strep (Gibco, Cat. 15140122)) containing 100 ng/mL Activin and 80 ng/mL FGF2.
513 On day four cells were fixed with 4% paraformaldehyde (Sigma, Cat. 158127) in DPBS and
514 were tested for markers of endoderm as described below.

515 For mesoderm, 100 ng/mL Activin, 20 ng/mL FGF2, 10 ng/mL BMP4, 10 μ M
516 LY294002, and 3 μ M CHIR99021 was supplemented to CDM-PVA for two days, with media
517 change each day. On day three cells were fixed with 4% paraformaldehyde in DPBS and
518 were tested for markers of mesoderm as described below.

519 For ectoderm, 10 nM SB431542 (Sigma, Cat. S4317-5MG), 12 ng/mL FGF2, and
520 150 ng/mL Noggin (Sigma, Cat. H6416-10UG) was supplemented to CDM-PVA medium for
521 ten days, with media change each day. On day eleven cells were fixed with 4%
522 paraformaldehyde in DPBS and were tested for markers of ectoderm as described below.

523 To assess differentiation capacity, samples were analysed using the 3-Germ Layer
524 Immunocytochemistry Kit (LifeTechnologies, Cat. A25538) per manufacturer's instructions.
525 TUJ1, AFP and SMA were included in this kit but anti-FoxA2/hHNF-Abs (diluted 1:100, R&D
526 Systems, Cat. AF2400), anti-Brachyury-Abs (diluted 1:100, R&D Systems, Cat. AF2085),
527 and anti-Nestin-Abs (diluted 1:100, Abcam, Cat. ab22035) were also acquired.

528 The next day, samples were incubated with the corresponding secondary Abs, which
529 were diluted 1:250 in 1% BSA in PBS. AFP, SMA, and TUJ1 were counter-stained with
530 AlexaFluor488 goat anti-mouse IgG1 (Invitrogen, Cat. A25536), AlexaFluor555 goat anti-
531 mouse IgG2a (Cat. A25533), and AlexaFluor647 donkey anti-rabbit (Invitrogen, Cat.
532 A25537), respectively from the 3-Germ Layer Immunocytochemistry Kit. FoxA2/hHNF and
533 Brachyury were counter-stained with mouse-anti-goat Texas Red (Santa Cruz
534 Biotechnology, Cat. sc-3916), and Nestin counter-stained with AlexaFluor 488 goat-anti
535 mouse (Invitrogen, Cat. A21121). After the secondary Ab incubation, the samples were
536 mounted using ProLongTM Diamond Antifade Mountant with DAPI (Invitrogen, Cat. P36971).
537 Images were taken with the CLSM Leica SP5 resonant APD at the Center for Microscopy
538 and Image Analysis, University of Zurich.

539

540 **Mature neuronal culture**

541 To generate neural progenitors, iPSCs were disassociated into single cells using
542 ACCUTASETM Cell detachment solution as described above, and seeded at high density
543 (1×10^6 cells per well of a 12-well plate) in SMAD inhibition medium as previously described
544²⁷. Cell counting was performed using the Countess 3 Automated Cell Counter
545 (ThermoFisher Scientific) with trypan blue (Gibco, Cat. 15250061) staining to identify dead
546 cells, as per manufacturer's instructions. Neural induction of iPSC was performed using the
547 STEMdiffTM SMADi Neural Induction Kit (StemCellTechnologies, Cat. 08582) and protocol
548 per manufacturer was followed²⁸. Briefly, iPSCs were cultured for 8-12 days on BME matrix
549 (as before) and passaged using 1 mg/mL Collagenase type IV solution (Gibco, Cat.
550 17104019) upon the appearance of neuroepithelial cells onto BME matrix coated 6-well

551 plates in STEMdiff™ SMADi Neural Induction medium. The next day, medium was switched
552 to neural maintenance medium (NMM: 48.4 mL KnockOut DMEM/F12, Gibco, Cat. 12660-
553 102; 48.5 mL Neurobasal, Gibco, Cat. 12348-017; 1 mL B-27 Supplement, Gibco, Cat.
554 17504-044; 500 µL N-2 Supplement, Gibco, Cat. 17502-048; 500 µL Non-essential amino
555 acids, Gibco, Cat. 11140-050; 500 µL GlutaMAX, Gibco, Cat. 35050-061; 500 µL Penicillin-
556 Streptomycin, Gibco, Cat. 15140-122; 90 µL 2-Mercaptoethanol, Gibco, Cat. 31350010; 25
557 µL Insulin solution, Sigma, Cat. I9278-5ML; as previously described²⁷) and henceforth
558 medium was refreshed daily. Upon formation of rosettes (as described in^{27,67}), cultures were
559 treated with 5 µL/mL Recombinant Human Basic Fibroblast Growth Factor (bFGF, 4 µg/mL,
560 Gibco, Cat. PHG0024). After four consecutive days of bFGF treatment, cells were passaged
561 with 1 mg/mL Collagenase type IV solution and transferred to BME matrix (Cultrex®) coated
562 6-plates. Once morphologically apparent neuronal cells (polarised with leading axon and
563 trailing dendrite) could be seen migrating from the apical border of the rosette, cultures were
564 passaged with ACCUTASE™ Cell detachment solution and plated onto 10 µg/mL laminin
565 (Sigma-Aldrich, Cat. L2020) and poly-L-Lysine (Sigma-Aldrich, Cat. P6282-5MG). Cells were
566 passaged between day 21 and 26, and either continued as neural cultures or frozen for
567 storage. For freezing, cells were detached using ACCUTASE™ Cell detachment solution,
568 transferred to neural freezing medium (90% NMM, 10% DMSO (Sigma, Cat. D2438), 20
569 ng/mL bFGF), and placed in a Mr. Frosty (Thermo Scientific, Cat. 5100-0001) at -80°C and
570 stored long-term in liquid nitrogen, as described²⁷.

571 Neural cultures were fed daily with NMM until day 45, after which 48-hour cycles
572 were implemented whereby every second day two thirds of the medium was removed and 2
573 mL NMM plus maturation supplements GDNF and BDNF (both at 20 ng/mL,
574 StemCellTechnologies, Cat. 78058 and 78005) were supplied to neuronal cultures. In this
575 way, neuronal cultures were maintained up to a maximum of day 120.

576
577

578 **Mitochondrial fluorometric stains and dyes**

579 Mitochondrial oxidative phosphorylation complex I was inhibited using 1 μ M rotenone
580 (Sigma, Cat. R8875-1G) in DMSO for 30 minutes added directly to the medium.
581 Mitochondrial membrane potential was assessed using tetramethylrhodamine-methyl-ester
582 perchlorate (Sigma, Cat. T668) reconstituted in DMSO and supplemented at 15 nM
583 incubated for 60 minutes. Mitochondrial superoxide production was measured using
584 MitoSOXTM Mitochondrial Superoxide Indicators (Invitrogen, Cat. M36008) reconstituted in
585 DMSO was supplemented at 5 μ M for 15 minutes.

586

587 **Electrophysiology**

588 Cells were used for electrophysiology studies after at least 50 days *in vitro* (range: 50 – 113,
589 mean: 73) and at least 20 days following addition of the maturation supplements GDNF and
590 BDNF in 10 μ g/mL laminin (Sigma-Aldrich, Cat. L2020) and transfer to poly-L-Lysine
591 (Sigma-Aldrich, Cat. P6282-5MG) coated NuncTM Cell Culture/Petri Dishes (Thermo
592 Scientific, Cat. 150318). For treatment studies, 0.1 mM, 6 mM or 12 mM dimethyl 2-
593 oxoglutarate (Sigma, Cat. 349631) (DM-2OG) was added for 24 hours before cell
594 collection. For recording, iPSC-derived neurons were placed in a recording chamber and
595 whole-cell patch-clamp recordings were performed using an EPC10 USB amplifier (HEKA).
596 iPSC-derived neurons were bathed with extracellular solution containing (in mM) 140 NaCl,
597 2 MgCl₂, 2 CaCl₂, 10 HEPES, 3 KCl, 10 D-Glucose, pH 7.4 (all from Sigma). Pipette solution
598 contained (in mM) 4 NaCl, 120 K-gluconate, 10 HEPES, 10 EGTA, 3 Mg-ATP, 0.5 CaCl₂, 1
599 MgCl₂ pH 7.2 (all from Sigma). Patch pipettes ~9 M Ω were pulled from borosilicate glass
600 capillaries (Harvard Apparatus, Cat. 30-0038). Voltages were corrected for a liquid junction
601 potential of +12 mV. Series resistance was not compensated.

602 We used current-clamp recordings to examine AP firing and membrane properties.
603 Step current injection protocols (duration, 2 s; step, 5 pA; -20 to +60 pA) were applied from
604 the neuron's resting membrane potential. Current-clamp data were filtered at 2.7 kHz and
605 digitized with 20–100 kHz. To study whole-cell currents, voltage steps (duration, 1 s) were
606 applied from a holding potential of -80 mV to voltages between -80 and +60 mV. Peak
607 inward and outward currents were quantified and normalized to whole-cell capacitance to
608 obtain current densities. Spontaneous excitatory postsynaptic currents were measured for
609 120 s at a holding potential of -80 mV. Voltage-clamp data were filtered at 2.9 kHz and
610 digitized with 50 kHz.

611 Where described, MitoTrackerTM Deep Red FM (Invitrogen, Cat. M22426) was used
612 at 0.1 μ M in NMM and provided directly to cells for 15 minutes. Thereafter, medium was
613 aspirated, and cells washed with extracellular solution. Tested doses of MitoTrackerTM Deep
614 Red FM \geq 1 μ M were not compatible with electrophysiological recording.

615 Electrophysiological data were analysed with custom-written routines in IgorPro
616 software (WaveMetrics, version 6.37) for current-clamp and voltage-clamp step protocols.
617 Spontaneous synaptic events were analysed using miniML⁶⁸ in Python (version 3.9).
618 Extracted data were integrated using R Studio (version 2022.12.0+353). Analysis scripts are
619 available upon request. Electrophysiology variables and groupings made during analysis are
620 summarised in Supplementary Tables 1 & 2.

621

622 **Transcriptomics**

623 Bulk RNA-seq was performed by Novogene from RNA extracted from liquid-nitrogen snap
624 frozen cell pellets (DIV range: 65 – 78, mean: 75) that were lysed using QIAshredder
625 (Qiagen, 79656) with RNA extracted using the RNeasy[®] Mini Kit (Qiagen, Cat. 74106). Prior
626 to sequencing, RNA quality was assessed using an ND-1000 Spectrophotometer (NanoDrop
627 Technologies, Inc.) to ensure sample purity was between A₂₆₀/280 = 1.8-2.2 and A₂₆₀/230
628 \geq 1.8. Peak illustration was conducted using an Agilent 5400 and the low marker was used
629 to calibrate the size of peaks. RNA libraries were prepared using poly(A) capture, followed
630 by reverse transcription into cDNA. Sequencing was performed in PE150 (paired-end 150)
631 mode on an Illumina NovaSeq 6000 at Novogene. Between 960 to 8800 ng of total RNA was
632 provided and \geq 20 million read pairs per sample were acquired.

633 Raw sequencing reads were preprocessed using the SUSHI framework^{69,70}, which
634 was developed by the Functional Genomics Center Zurich (FGCZ). Adapter sequences and
635 low-quality reads were trimmed off using fastp v0.02⁷⁰. Filtered reads were pseudo-aligned
636 against the reference human genome assembly GRCh38.p13 and quantified using Kallisto
637 v0.46.1⁷¹. Differential gene expression analysis was performed between different conditions
638 using the R package edgeR v3.42⁷². 21057 features were identified, and 15530 features
639 had counts above the threshold. $P < 0.05$ (reported as false discovery rate unless otherwise
640 stated, correction is done via Benjamini-Hochberg method) and one-fold change were
641 considered to be differentially expressed. R package clusterProfiler was used for functional
642 enrichment analysis based on Go terms and KEGG pathways, which utilised Over-
643 Representation Analysis⁷³.

644

645 **Pseudo sc-RNaseq**

646 To determine the cell type abundance, we used a deconvolution approach on the
647 bulk gene expression profiles of the iPSC-derived neurons collected as described in
648 Transcriptomics method section. We used the machine learning method CIBERSORTx⁷⁴ to
649 infer cell-type proportion without physical cell isolation. With CIBERSORTx⁷⁴, we created a
650 signature matrix of cell type identified in iPSC-derived neurons using published single-cell
651 RNA-sequencing data by Gutierrez-Franco *et al*⁷⁵, wherein the same iPSC differentiation
652 protocol was used. Using this fine single-cell annotation of iPSC-derived neurons, we could
653 run this digital cytometry tool on bulk transcriptomic expression to estimate cell type
654 abundances.

655

656 **Metabolomics – Sugar phosphates**

657 Polar metabolites were extracted from neuronal cells at day 60 cultured in 6-well plates,
658 either untreated or after 24 hours supplementation with 12 mM DM-2OG, according to the
659 described protocol⁷⁶. After extraction, the metabolites were concentrated and dried via an
660 Alpha 3-4 LSCbasic (Martin Christ, 102394, 102395) in vacuo centrifuge with an external oil-
661 pump overnight at ambient temperature and stored at -80°C until analysis.

662 The metabolite extracts were dissolved in 100 μ L of ultrapure water upon analysis,
663 and a volume of 8 μ L per sample was injected into an Agilent 1290 ultra-high performance
664 liquid chromatography (UHPLC) module connect to an Agilent 6490A tandem quadrupole
665 (QqQ) mass spectrometer, as previously described³². Chromatography was performed using
666 a 0.25 μ L/min flow rate and a gradient from 0 to 100% mobile phase B over a 25-minute total
667 run time. Mobile phase A (12 mM acetic acid, 10 mM tetrabutylammonium, 2 mM
668 acetylacetone, 3% methanol in mQ) and B (12 mM acetic acid, 10 mM tetrabutylammonium,
669 2 mM acetylacetone, 3% methanol, 80% acetonitrile in mQ) were used for phosphate sugar
670 separation. The gradient method was as follows (time: % B): 11 min: 0%; 14 min: 15%; 19
671 min: 40%; 20 min: 100%; 21.5 minutes 0%. The QqQ MS was operated in dynamic multiple-
672 reaction monitoring (MRM) mode. The list of transitions used to detect targeted compounds
673 is reported in Supplementary Table 3. Skyline Software (v20.2, MacCoss Lab Software) was
674 used for peak integration and resulting peak areas were normalized on total peak area³².
675 Data processing and statistical data analysis were performed in PRISM GraphPad (v.5.03).
676 Technical triplicates were measured for each sample. Shapiro-Wilk test was used to assess
677 normality. Significance was evaluated for multiple comparison via Kruskal-Wallis test with
678 significance set at $p < 0.05$ (without post hoc correction).

679 The normalization of the MS data for the TBA-based analysis was performed using
680 the total peak area method, by dividing the area of the peak of interest by the sum of the
681 areas of all peaks included in the analysis (as normalization factor), to derive relative
682 abundances. The resulting relative abundances of the target compounds are thus unitless
683 number, meaning a pure quantity without a physical unit.

684 This normalization method is widely used in MS-based metabolomics^{32,77-80}, and it is
685 particularly useful when the protein concentration of samples as estimation of the initial
686 biomass cannot be determined due to the metabolite extraction protocol employed, as in the
687 case of our study.

688 A complete list of metabolites detected, and their transition information, is available in
689 Supplementary Table 3.
690

691 **Metabolomics – TCA cycle metabolites and stable isotope tracing**

692 Treated cells were supplemented with 12 mM DM-2OG for 24 hours. Four hours before cell
693 collection, medium was changed to NMM without GlutaMAX™ Supplement (Gibco, Cat.
694 35050061) and with 4 mM [$U-^{13}C$] glutamine (Sigma-Aldrich, Cat. 605166). At collection,
695 medium was removed, coverslips quickly dipped into sterile double-distilled water at 37°C
696 and quenched in 80% methanol at -20°C. Cells were scrapped in methanol and
697 centrifuged at 15,000g for 15 minutes at 4°C. Supernatants were collected, snap-frozen in
698 liquid nitrogen and stored at -80°C before LC-MS analysis. Mass spectrometry
699 preparation and processing was performed as previously described¹⁰.
700

701 **Immunocytochemistry**

702 To detect native protein markers, immunochemical assay was performed on cells grown on
703 glass coverslips treated with poly-L-Lysine. Depending on cell state, coverslips were also
704 treated with BME matrix (iPSCs, NECs, NSCs) or laminin (NPCs, Neurons). Briefly, cells
705 were washed with DPBS (Gibco, Cat. 14190144), and fixed with 4% paraformaldehyde
706 (Sigma-Aldrich, Cat. 158127) in DPBS for 15 minutes at ambient temperature. Cells were
707 then permeabilised for 30 minutes in 0.1% triton (diluted in DPBS), PFA was quenched
708 using 100 mM glycine solution for 15 minutes, and coverslips blocked in 1% BSA for 60
709 minutes. Both primary and secondary antibodies were diluted in 1% BSA. All solutions were
710 prepared in DPBS. A full list of antibodies, their sources, dilution ratios, incubation times and
711 manufacturers can be found in Supplementary Table 4.
712

713 **Imaging and microscopy**

714 Immunofluorescence images, unless otherwise stated, were taken with a DMi8 S Inverted
715 Microscope fitted with a DFC480 camera (Leica) and RGB filter boxes. Image acquisition
716 was adjusted for each fluorophore-antibody combination. All cells, unless otherwise stated,
717 were plated on glass coverslips (Epredia, Cat. 630-2124) treated with poly-L-Lysine (Sigma-
718 Aldrich, Cat. P6282-5MG) and mounted on Adhesive Microscopic Slides 25 x 75mm Menzel
719 (ThermoFisher, Cat. J1800AMNZ) with either ProLong™ Gold Antifade Mountant with DNA
720 Stain DAPI (Invitrogen, Cat. P36935) or ProLong™ Gold Antifade Mountant without DAPI
721 (Invitrogen, Cat. P10144).

722 Images were also acquired using a Leica Confocal SP8 Inverse Falcon with Power
723 HyD R photon detector in counting mode, and fluorophores excited using a white light laser
724 or photomultiplier tube with a 405 diode to excite fluorophores in the UV spectrum. Images
725 were acquired using an HC PL APO 63x/1.40 OIL CS2 objective (Leica) with oil immersion
726 liquid ("Type-F" immersion liquid, Leica). Acquisition parameters for high resolution images
727 and deconvolution: Z-step at 130 nm (Image slices range 18-25), Image size at 42.91 µm.
728 Image deconvolution was performed using Bitplane Imaris.
729

730 **Correlation colocalization image analysis**

731 The analysis of colocalization of the MMUT and TOMM20 channels was performed using the
732 Coloc 2 plugin in ImageJ. This plugin performed a spatial pixel intensity correlation, creating
733 a scatterplot with a linear regression fit, which indicated the degree of colocalization between
734 the two channels. Pearson's correlation analysis and the calculated Pearson's R coefficient
735 were extracted and reported, (https://imagej.net/Coloc_2 and
736 https://imagej.net/Colocalization_Analysis).

737 **Immunoblotting**

738 Cells were collected with Accutase or scraping, washed with DPBS, and centrifuged to
739 retrieve pellets. The supernatant was removed, and the remaining pellet was either used
740 immediately for the lysate production or stored at -80°C for a later use. The cell pellets were
741 resuspended in 100 µl of lysis buffer containing 150 mM NaCl (Sigma, Cat.#S7653), 50 mM
742 Trizma-Base (pH 8, Sigma, Cat.#T1503), 1% NP-40 (IGEPAL CA-630, Sigma, Cat.#I8896),
743

744 10% sodium deoxycholate (Sigma, Cat.#D6750) and 1% Halt™ Protease & Phosphatase
745 Inhibitor Cocktail (100X, Thermo Fischer Scientific, Cat.#78440) and centrifuged max speed
746 at 4°C for 5 minutes. The supernatant was collected in a pre-cooled microfuge tube. The
747 protein concentration of each sample was assessed by performing a Bradford assay (Quick
748 Start Bradford 1X Dye Reagent, BioRad, Cat.#5000205) and measuring the absorbance at
749 595 nm. The samples were prepared by adding the protein extract to a mixture of lysis buffer
750 and 4X Laemmli buffer (BioRad, Cat.#161-0747) with 5% β-Mercaptoethanol (Sigma,
751 Cat.#M6250) to obtain a total protein concentration of 1 µg/µL. The samples were incubated
752 at 96°C for 5 minutes, before 15 µg was loaded, alongside a molecular weight standard
753 (PageRuler™ Plus Prestained Protein Ladder, Thermo Fischer Scientific, Cat.#26619) on
754 Novex™ Tris-Glycine Mini Protein Gels, 4–20%, 1.0 mm, WedgeWell™ format (Invitrogen,
755 XP04200BOX) or self-cast 12% running gel (in µL: 2500 H₂O, 3000 Bis-Acrylamide (Bio-
756 Rad, Cat.#1610158) 30:0.8, 1875 1.5M Tris-HCl (pH 8.8), 75 10% SDS, 50 10% APS, 5
757 TEMED). The 10x running running buffer comprised 1.92 M glycine (PanReac AppliChem,
758 Cat.#A1067,1000), 250 mM Trizma-Base and 35 mM Sodium dodecyl sulfate (SDS, Sigma,
759 Cat.#L3771), which were dissolved in double-distilled water. The gels were run at 140V until
760 the sample front reached the end of the gel. Proteins were transferred onto a nitrocellulose
761 (pore size 0.45 µm; Cytiva, Cat.#10600007) or polyvinylidene fluoride (pore size 0.22 µm,
762 activated in MeOH; Bio-Rad, Cat.#1620177) blotting membrane using the Trans-Blot®
763 TurboTM Transfer Pack in running buffer + 20% methanol with Bio-Rad standard program
764 (30 mins). Ponceau staining (Sigma, Cat.#P7170-1L) was performed to visualise protein
765 transfer. Ponceau solution was washed off with distilled water and the membrane was
766 blocked in blocking buffer at ambient temperature (10% 10x TBS-tween (24 g Tris base, 88
767 g NaCl (Sigma, Cat.#71380-1kG), in 1L distilled water neutralised to pH 7.6 with HCl) 0.2%
768 Tween (Sigma, Cat.#P1379-100ML), 5% milk powder (Millipore, Cat.#70166-500G)) for 1
769 hour. Antibody staining was performed with agitation for 2 hours in ambient conditions or
770 overnight at 4°C. Membranes were washed in 1xTBS-tween in between each step. Stained
771 protein signal was developed using Cytiva GE ECL Solution (Amersham, RPN2109) or
772 Clarity Max ECL solution (Bio-Rad, 1705062) on the ChemiDoc™ Touch imaging system
773 (Bio-Rad). A full list of antibodies, their sources, dilution ratios, incubation times and
774 manufacturers can be found in Supplementary Table 4. Uncropped gels can be found in
775 Supplementary Figure 12.

776

777 **Propionate Incorporation Assay**

778

779 The assay to quantify propionate pathway catabolism of iPSCs was assessed according to a
780 protocol described previously⁸¹ and included modifications as described²⁶.

781

782 **Quantitative PCR**

783

784 To test for incorporation of remnants of the Sendai virus, RNA was extracted from
785 fibroblasts, Sendai virus-positive fibroblasts and iPSCs using either the QIAamp RNA Blood
786 Mini Kit (QIAGEN) or Qiagen RNeasy micro kit (QIAGEN) following manufacturer's
787 instructions. The isolated RNA was converted into cDNA, utilizing PrimeScript™ 1st strand
788 cDNA Synthesis Kit (Takara, Cat.#6210A). cDNA was amplified by PCR, using Taq
789 Polymerase (New England Biolabs) using the primers listed in Supplementary table 5. The
790 PCR products were stained with EZ-Vision® One DNA Dye as Loading Buffer, 6X
791 (Amresco), analyzed by gel electrophoresis on a 2% agarose gel and visualized by an UV
792 transilluminator (Alpha Imager HP).

793

794 To test for expression of SOX2, PAX6 and EOMES, RNA was extracted from iPSC,
795 neuroepithelium and NSCs as described above. cDNA was synthesised from 500-3000 ng
796 RNA using the PrimeScriptTM II 1st Strand cDNA Synthesis Kit using a Professional TRIO
797 Thermocycler (Analytik Jena) following manufacturer's instructions. Real-time quantitative
798 PCR (RT-qPCR) consisted of 10 µL of GoTaq® qPCR Master Mix (2X, Promega,
799 Cat.#A600A), 5 µL diethylpyrocarbonate (DEPC BioChemica, PanReac AppliChem,
Cat.#A0881,0020) treated water and 1 µL of a 10 mM solution containing forward and
reverse primers for the genes of interest, to which 4 µL of 300-3000 ng cDNA were added.
The RT-qPCR was performed using either a LightCycler® 480 II (Roche), a 7900HT Fast

800 Real-Time PCR System (Applied Biosystems), or a QuantStudio™ 7 Pro Flex Real-Time
801 PCR System (Applied Biosystems, 4485701). In all cases the following conditions were
802 used: 96°C for 5 minutes, followed by 45 cycles composed of 10 seconds at 96°C and 1
803 minute at 60°C. Technical triplicates were performed for each sample. Data were collected
804 using the LightCycler® 480 Software release 1.5.0 SP4 or exported from the QuantStudio as
805 CSV. The relative gene expressions were normalized using the housekeeping gene β -actin
806 and analysed using the $2^{-\Delta\Delta C_t}$ method⁸². Primer sequences can be found in Supplementary
807 Table 5.

808

809 **Statistics and Reproducibility**

810 Where necessary statistical testing is noted in the respective figure legend. Descriptive
811 values and cell sources have been included in all figure legends. All datapoints have been
812 displayed and what they represent is clearly stated.

813

814 **Data availability**

815 All main data supporting the findings of this study are available within the article,
816 Supplementary Data, and Supplementary Figures. RNA sequencing data have been
817 deposited in Gene Expression Omnibus under the access number GSE289294. Source data
818 can be found in Supplementary Data. Unprocessed blots can be found in Supplementary
819 Figure 12. All other data are available from the corresponding author (or other sources, as
820 applicable) on reasonable request.

821

822

823 **References**

- 824 1. Rath, S. *et al.* MitoCarta3.0: an updated mitochondrial proteome now with sub-organelle
825 localization and pathway annotations. *Nucleic Acids Res.* **49**, D1541–D1547 (2021).
- 826 2. Schaefer, A., Lim, A. & Gorman, G. Epidemiology of Mitochondrial Disease. in *Diagnosis*
827 and *Management of Mitochondrial Disorders* (eds. Mancuso, M. & Klopstock, T.) 63–79
828 (Springer International Publishing, Cham, 2019). doi:10.1007/978-3-030-05517-2_4.
- 829 3. Rahman, S. Mitochondrial disease in children. *J. Intern. Med.* **287**, 609–633 (2020).
- 830 4. Rahman, J. & Rahman, S. Mitochondrial medicine in the omics era. *Lancet Lond. Engl.*
831 **391**, 2560–2574 (2018).
- 832 5. Wajner, M. Neurological manifestations of organic acidurias. *Nat. Rev. Neurol.* **15**, 253–
833 271 (2019).
- 834 6. DiMauro, S. & Schon, E. A. Mitochondrial disorders in the nervous system. *Annu. Rev.*
835 *Neurosci.* **31**, 91–123 (2008).
- 836 7. Chinnery, P. F. Primary Mitochondrial Disorders Overview. in *GeneReviews®* (eds.
837 Adam, M. P. *et al.*) (University of Washington, Seattle, Seattle (WA), 1993).
- 838 8. Forny, P. *et al.* Guidelines for the diagnosis and management of methylmalonic
839 aciduria and propionic aciduria: First revision. *J. Inherit. Metab. Dis.* **44**, 566–592
840 (2021).
- 841 9. Froese, D. S. & Gravel, R. A. Genetic disorders of vitamin B12 metabolism: eight
842 complementation groups – eight genes. *Expert Rev. Mol. Med.* **12**, e37 (2010).
- 843 10. Forny, P. *et al.* Integrated multi-omics reveals anaplerotic insufficiency in methylmalonyl-
844 CoA mutase deficiency. (2023) doi:<https://doi.org/10.1038/s42255-022-00720-8>.
- 845 11. Kölker, S. *et al.* no Methylmalonic acid, a biochemical hallmark of methylmalonic
846 acidurias but no inhibitor of mitochondrial respiratory chain. *J. Biol. Chem.* **278**, 47388–
847 47393 (2003).
- 848 12. Luciani, A. *et al.* Impaired mitophagy links mitochondrial disease to epithelial stress in
849 methylmalonyl-CoA mutase deficiency. *Nat. Commun.* **11**, 970 (2020).
- 850 13. de Keyzer, Y. *et al.* Multiple OXPHOS deficiency in the liver, kidney, heart, and skeletal
851 muscle of patients with methylmalonic aciduria and propionic aciduria. *Pediatr. Res.* **66**,
852 91–95 (2009).
- 853 14. Collado, M. S. *et al.* Biochemical and anaplerotic applications of in vitro models of
854 propionic acidemia and methylmalonic acidemia using patient-derived primary
855 hepatocytes. *Mol. Genet. Metab.* **130**, 183–196 (2020).
- 856 15. Wongkittichote, P. *et al.* Tricarboxylic acid cycle enzyme activities in a mouse model of
857 methylmalonic aciduria. *Mol. Genet. Metab.* **128**, 444–451 (2019).
- 858 16. Chandler, R. J. *et al.* Mitochondrial dysfunction in mut methylmalonic acidemia. *FASEB J.* **23**,
859 1252–1261 (2009).
- 860 17. Manoli, I. *et al.* Targeting proximal tubule mitochondrial dysfunction attenuates the renal
861 disease of methylmalonic acidemia. *Proc. Natl. Acad. Sci.* **110**, 13552–13557 (2013).
- 862 18. Ramon, C., Traversi, F., Bürer, C., Froese, D. S. & Stelling, J. No Cellular and
863 computational models reveal environmental and metabolic interactions in MMUT-type
864 No methylmalonic aciduria. *J. Inherit. Metab. Dis.* **n/a**.
- 865 19. Kandel, E. R., Koester, J. D., Mack, S. H. & Siegelbaum, S. A. Synaptic Transmission. in
866 *Principles of Neural Science*, 6e (McGraw Hill, New York, NY, 2021).
- 867 20. Zheng, X. *et al.* Metabolic reprogramming during neuronal differentiation from aerobic
868 glycolysis to neuronal oxidative phosphorylation. *eLife* **5**, e13374 (2016).
- 869 21. Yellen, G. Fueling thought: Management of glycolysis and oxidative phosphorylation in
870 neuronal metabolism. *J. Cell Biol.* **217**, 2235–2246 (2018).
- 871 22. Bouzier-Sore, A.-K. *et al.* Competition between glucose and lactate as oxidative energy
872 substrates in both neurons and astrocytes: a comparative NMR study. *Eur. J. Neurosci.*
873 **24**, 1687–1694 (2006).
- 874 23. Hall, C. N., Klein-Flügge, M. C., Howarth, C. & Attwell, D. Oxidative Phosphorylation, Not
875 Glycolysis, Powers Presynaptic and Postsynaptic Mechanisms Underlying Brain
876 Information Processing. *J. Neurosci.* **32**, 8940–8951 (2012).

877 24. Forny, P. *et al.* Molecular Genetic Characterization of 151 Mut-Type Methylmalonic
878 Aciduria Patients and Identification of 41 Novel Mutations in MUT. *Hum. Mutat.* **37**, 745–
879 754 (2016).

880 25. Acquaviva, C. *et al.* N219Y, a new frequent mutation among mut^o forms of
881 methylmalonic aciduria in Caucasian patients. *Eur. J. Hum. Genet.* **9**, 577–582 (2001).

882 26. Froese, S. & Baumgartner, M. Lysosomal Vitamin B12 Trafficking. in *Ion and Molecule*
883 *Transport in Lysosomes* (CRC Press, 2020).

884 27. Shi, Y., Kirwan, P. & Livesey, F. J. Directed differentiation of human pluripotent stem
885 cells to cerebral cortex neurons and neural networks. *Nat. Protoc.* **7**, 1836–1846 (2012).

886 28. Chambers, S. M. *et al.* Highly efficient neural conversion of human ES and iPS cells by
887 dual inhibition of SMAD signaling. *Nat. Biotechnol.* **27**, 275–280 (2009).

888 29. Wurm, C. A. *et al.* Nanoscale distribution of mitochondrial import receptor Tom20 is
889 adjusted to cellular conditions and exhibits an inner-cellular gradient. *Proc. Natl. Acad.*
890 *Sci.* **108**, 13546–13551 (2011).

891 30. Bardy, C. *et al.* Predicting the functional states of human iPSC-derived neurons with
892 single-cell RNA-seq and electrophysiology. *Mol. Psychiatry* **21**, 1573–1588 (2016).

893 31. Inak, G. *et al.* Defective metabolic programming impairs early neuronal morphogenesis
894 in neural cultures and an organoid model of Leigh syndrome. *Nat. Commun.* **12**, 1929
895 (2021).

896 32. van Scherpenzeel, M. *et al.* Dynamic tracing of sugar metabolism reveals the
897 mechanisms of action of synthetic sugar analogs. *Glycobiology* **32**, 239–250 (2022).

898 33. Fan, J. *et al.* Glutamine-□ driven oxidative phosphorylation is a major ATP source in
899 transformed mammalian cells in both normoxia and hypoxia. *Mol. Syst. Biol.* **9**, 712
900 (2013).

901 34. WU, G., HAYNES, T. E., LI, H., YAN, W. & MEININGER, C. J. Glutamine metabolism to
902 glucosamine is necessary for glutamine inhibition of endothelial nitric oxide synthesis.
903 *Biochem. J.* **353**, 245–252 (2001).

904 35. Hansen, K. B. *et al.* Structure, Function, and Pharmacology of Glutamate Receptor Ion
905 Channels. *Pharmacol. Rev.* **73**, 298–487 (2021).

906 36. Hayasaka, K. *et al.* Comparison of Cytosolic and Mitochondrial Enzyme Alterations in
907 the Livers of Propionic or Methylmalonic Acidemia: A Reduction of Cytochrome Oxidase
908 Activity. *Tohoku J. Exp. Med.* **137**, 329–334 (1982).

909 37. Martinelli, D. *et al.* Neurologic outcome following liver transplantation for methylmalonic
910 aciduria. *J. Inherit. Metab. Dis.* **n/a**.

911 38. Kaplan, P., Ficicioglu, C., Mazur, A. T., Palmieri, M. J. & Berry, G. T. Liver
912 transplantation is not curative for methylmalonic acidopathy caused by methylmalonyl-
913 CoA mutase deficiency. *Mol. Genet. Metab.* **88**, 322–326 (2006).

914 39. Molema, F. *et al.* Neurotoxicity including posterior reversible encephalopathy syndrome
915 after initiation of calcineurin inhibitors in transplanted methylmalonic acidemia patients:
916 Two case reports and review of the literature. *JIMD Rep.* **51**, 89–104 (2020).

917 40. Chakrapani, A., Sivakumar, P., McKiernan, P. J. & Leonard, J. V. Metabolic stroke in
918 methylmalonic aciduria five years after liver transplantation. *J. Pediatr.* **140**, 261–263
919 (2002).

920 41. Kasahara, M. *et al.* Current role of liver transplantation for methylmalonic aciduria: A
921 review of the literature. *Pediatr. Transplant.* **10**, 943–947 (2006).

922 42. Nyhan, W. L., Gargus, J. J., Boyle, K., Selby, R. & Koch, R. Progressive neurologic
923 disability in methylmalonic aciduria despite transplantation of the liver. *Eur. J. Pediatr.*
924 **161**, 377–379 (2002).

925 43. Mc Guire, P. J. *et al.* Combined liver–kidney transplant for the management of
926 methylmalonic aciduria: A case report and review of the literature. *Mol. Genet. Metab.*
927 **93**, 22–29 (2008).

928 44. Galera-Monge, T. *et al.* Mitochondrial Dysfunction and Calcium Dysregulation in Leigh
929 Syndrome Induced Pluripotent Stem Cell Derived Neurons. *Int. J. Mol. Sci.* **21**, 3191
930 (2020).

931 45. Jung, H.-Y., Mickus, T. & Spruston, N. Prolonged Sodium Channel Inactivation
932 Contributes to Dendritic Action Potential Attenuation in Hippocampal Pyramidal Neurons.
933 *J. Neurosci.* **17**, 6639–6646 (1997).

934 46. Groten, C. J. & MacVicar, B. A. Mitochondrial Ca²⁺ uptake by the MCU facilitates
935 pyramidal neuron excitability and metabolism during action potential firing. *Commun.*
936 *Biol.* **5**, 1–15 (2022).

937 47. Chang, D. T. W., Honick, A. S. & Reynolds, I. J. Mitochondrial trafficking to synapses in
938 cultured primary cortical neurons. *J. Neurosci. Off. J. Soc. Neurosci.* **26**, 7035–7045
939 (2006).

940 48. McKenna, M. C. The glutamate-glutamine cycle is not stoichiometric: Fates of glutamate
941 in brain. *J. Neurosci. Res.* **85**, 3347–3358 (2007).

942 49. Aldana, B. I. *et al.* Glutamate-glutamine homeostasis is perturbed in neurons and
943 astrocytes derived from patient iPSC models of frontotemporal dementia. *Mol. Brain* **13**,
944 125 (2020).

945 50. Andersen, J. V. *et al.* Deficient astrocyte metabolism impairs glutamine synthesis and
946 neurotransmitter homeostasis in a mouse model of Alzheimer's disease. *Neurobiol. Dis.*
947 **148**, 105198 (2021).

948 51. Shen, J. *et al.* Determination of the rate of the glutamate/glutamine cycle in the human
949 brain by in vivo ¹³C NMR. *Proc. Natl. Acad. Sci.* **96**, 8235–8240 (1999).

950 52. Chen, Q. *et al.* Rewiring of Glutamine Metabolism Is a Bioenergetic Adaptation of
951 Human Cells with Mitochondrial DNA Mutations. *Cell Metab.* **27**, 1007–1025.e5 (2018).

952 53. Yoo, H. C., Yu, Y. C., Sung, Y. & Han, J. M. Glutamine reliance in cell metabolism. *Exp.*
953 *Mol. Med.* **52**, 1496–1516 (2020).

954 54. Conte, F., van Buuringen, N., Voermans, N. C. & Lefeber, D. J. Galactose in human
955 metabolism, glycosylation and congenital metabolic diseases: Time for a closer look.
956 *Biochim. Biophys. Acta BBA - Gen. Subj.* **1865**, 129898 (2021).

957 55. Lissin, D. V., Carroll, R. C., Nicoll, R. A., Malenka, R. C. & Zastrow, M. von. Rapid,
958 Activation-Induced Redistribution of Ionotropic Glutamate Receptors in Cultured
959 Hippocampal Neurons. *J. Neurosci.* **19**, 1263–1272 (1999).

960 56. Lu, W.-Y. *et al.* Activation of Synaptic NMDA Receptors Induces Membrane Insertion of
961 New AMPA Receptors and LTP in Cultured Hippocampal Neurons. *Neuron* **29**, 243–254
962 (2001).

963 57. Mosbacher, J. *et al.* A Molecular Determinant for Submillisecond Desensitization in
964 Glutamate Receptors. *Science* **266**, 1059–1062 (1994).

965 58. Zhu, J. J., Esteban, J. A., Hayashi, Y. & Malinow, R. Postnatal synaptic potentiation:
966 Delivery of GluR4-containing AMPA receptors by spontaneous activity. *Nat. Neurosci.* **3**,
967 1098–1106 (2000).

968 59. Ballhausen, D., Mittaz, L., Boulat, O., Bonafé, L. & Braissant, O. Evidence for catabolic
969 pathway of propionate metabolism in CNS: expression pattern of methylmalonyl-CoA
970 mutase and propionyl-CoA carboxylase alpha-subunit in developing and adult rat brain.
971 *Neuroscience* **164**, 578–587 (2009).

972 60. Head, P. E. *et al.* Aberrant methylmalonylation underlies methylmalonic acidemia and is
973 attenuated by an engineered sirtuin. *Sci. Transl. Med.* **14**, eabn4772 (2022).

974 61. Bian, Y. *et al.* An enzyme assisted RP-RPLC approach for in-depth analysis of human
975 liver phosphoproteome. *J. Proteomics* **96**, 253–262 (2014).

976 62. Patterson, K., Linask, K. L., Beers, J. & Zou, J. Generation of two tdTomato reporter
977 induced pluripotent stem cell lines (NHLBli003-A-1 and NHLBli003-A-2) by AAVS1 safe
978 harbor gene-editing. *Stem Cell Res.* **42**, 101673 (2020).

979 63. Chichagova, V., Sanchez-Vera, I., Armstrong, L., Steel, D. & Lako, M. Generation of
980 Human Induced Pluripotent Stem Cells Using RNA-Based Sendai Virus System and
981 Pluripotency Validation of the Resulting Cell Population. *Methods Mol. Biol. Clifton NJ*
982 **1353**, 285–307 (2016).

983 64. Ghaedi, M. & Niklason, L. E. Human Pluripotent Stem Cells (iPSC) Generation, Culture,
984 and Differentiation to Lung Progenitor Cells. *Methods Mol. Biol. Clifton NJ* **1576**, 55–92
985 (2019).

986 65. Vallier, L. & Pedersen, R. Differentiation of human embryonic stem cells in adherent and
987 in chemically defined culture conditions. *Curr. Protoc. Stem Cell Biol. Chapter 1*, Unit
988 1D.4.1-1D.4.7 (2008).

989 66. Vallier, L. *et al.* Early Cell Fate Decisions of Human Embryonic Stem Cells and Mouse
990 Epiblast Stem Cells Are Controlled by the Same Signalling Pathways. *PLoS ONE* **4**,
991 e6082 (2009).

992 67. Shi, Y., Kirwan, P., Smith, J., Robinson, H. P. C. & Livesey, F. J. No Human cerebral
993 cortex development from pluripotent stem cells to functional excitatory synapses. *Nat.*
994 *Neurosci.* **15**, 10.1038/nrn.3041 (2012).

995 68. O'Neill, P. S. *et al.* Deep learning-based synaptic event detection. 2023.11.02.565316
996 Preprint at <https://doi.org/10.1101/2023.11.02.565316> (2023).

997 69. Hatakeyama, M. *et al.* SUSHI: an exquisite recipe for fully documented, reproducible and
998 reusable NGS data analysis. *BMC Bioinformatics* **17**, 228 (2016).

999 70. Chen, S., Zhou, Y., Chen, Y. & Gu, J. fastp: an ultra-fast all-in-one FASTQ preprocessor.
1000 *Bioinforma. Oxf. Engl.* **34**, i884–i890 (2018).

1001 71. Bray, N. L., Pimentel, H., Melsted, P. & Pachter, L. Near-optimal probabilistic RNA-seq
1002 quantification. *Nat. Biotechnol.* **34**, 525–527 (2016).

1003 72. Robinson, M. D., McCarthy, D. J. & Smyth, G. K. edgeR: a Bioconductor package for
1004 differential expression analysis of digital gene expression data. *Bioinforma. Oxf. Engl.*
1005 **26**, 139–140 (2010).

1006 73. Yaari, G., Bolen, C. R., Thakar, J. & Kleinstein, S. H. Quantitative set analysis for gene
1007 expression: a method to quantify gene set differential expression including gene-gene
1008 correlations. *Nucleic Acids Res.* **41**, e170 (2013).

1009 74. Newman, A. M. *et al.* Determining cell type abundance and expression from bulk tissues
1010 with digital cytometry. *Nat. Biotechnol.* **37**, 773–782 (2019).

1011 75. Gutiérrez-Franco, A. *et al.* Methanol fixation is the method of choice for droplet-based
1012 single-cell transcriptomics of neural cells. *Commun. Biol.* **6**, 1–12 (2023).

1013 76. Conte, F. *et al.* In Vitro Skeletal Muscle Model of PGM1 Deficiency Reveals Altered
1014 Energy Homeostasis. *Int. J. Mol. Sci.* **24**, 8247 (2023).

1015 77. Ruiz-Hernández, V., Roca, M. J., Egea-Cortines, M. & Weiss, J. A comparison of semi-
1016 quantitative methods suitable for establishing volatile profiles. *Plant Methods* **14**, 67
1017 (2018).

1018 78. Sun, J. & Xia, Y. Pretreating and normalizing metabolomics data for statistical analysis.
1019 *Genes Dis.* **11**, 100979 (2024).

1020 79. Conte, F. *et al.* Isotopic Tracing of Nucleotide Sugar Metabolism in Human Pluripotent
1021 Stem Cells. *Cells* **12**, 1765 (2023).

1022 80. Guezenoc, J., Gallet-Budynek, A. & Bousquet, B. Critical review and advices on
1023 spectral-based normalization methods for LIBS quantitative analysis. *Spectrochim. Acta
1024 Part B At. Spectrosc.* **160**, 105688 (2019).

1025 81. Willard, H. F., Ambani, L. M., Hart, A. C., Mahoney, M. J. & Rosenberg, L. E. Rapid
1026 prenatal and postnatal detection of inborn errors of propionate, methylmalonate, and
1027 cobalamin metabolism: A sensitive assay using cultured cells. *Hum. Genet.* **34**, 277–283
1028 (1976).

1029 82. Livak, K. J. & Schmittgen, T. D. Analysis of relative gene expression data using real-time
1030 quantitative PCR and the 2(-Delta Delta C(T)) Method. *Methods San Diego Calif* **25**,
1031 402–408 (2001).

1032
1033 **Acknowledgements**

1034 The authors thank Adhideb Ghosh for his assistance with transcriptomic data and Caroline
1035 Frei for her assistance with development of R analysis script. MCSD was supported by the
1036 FZK Fellowship of the University Children's Hospital Zurich. DSF is supported by the Swiss
1037 National Science Foundation [310030_192505] and the University Research Priority
1038 Program of the University of Zurich ITINERARE – Innovative Therapies in Rare Diseases.
1039 MRB is supported by the Swiss National Science Foundation [310030_175779] and

1040 310030_212505] and the University Research Priority Program of the University of Zurich
1041 ITINERARE – Innovative Therapies in Rare Diseases.

1042

1043 **Author contributions**

1044 MCSD, DSF, and MRB contributed to the conception and design of the study. MCSD carried
1045 out the experimental work contributing to the majority of the paper. MCSD and DSF
1046 prepared
1047 the manuscript with input from the other authors. MS generated patient-derived iPSCs. GM
1048 performed western blots and ICC. MAG performed western blots. DPR performed
1049 electrophysiology and ID helped with analysis and wrote some of the analysis scripts. MP
1050 performed TCA cycle metabolomics. FC performed HexP metabolomics. BV and FvM
1051 facilitated bulk transcriptomics and data integration. SC conducted bulk RNAseq
1052 deconvolution. All authors contributed to the manuscript and approved the submitted
1053 version.

1054

1055 **Competing interests**

1056 All authors declare no competing interests.

1057

1058 **Correspondence and requests for materials** should be addressed to D. Sean Froese, or
1059 Matthias R. Baumgartner

1060

1061 Figure Caption, Main figure 1:
1062 **Generation of iPSC-derived MMUT-deficient neurons from individuals with**
1063 **methylmalonic aciduria.** **a**, Schematic of the affected metabolic pathway in MMUT
1064 deficiency. Created in BioRender. **b**, Brightfield and epifluorescent acquisitions of
1065 pluripotency (NANOG, SSEA4, SOX2) and proliferation (Ki67) markers in representative
1066 iPSC cultures from control and patient lines. Scale, 50 μ m. **c**, Ectoderm lineage indicated by
1067 beta-tubulin III (TUJ1) and nestin (NES) positive cells after 12 days *in vitro* (DIV). Endoderm
1068 lineage indicated by anti- α -Fetoprotein (AFP) positive cells after 4 days *in vitro* (DIV).
1069 Mesoderm lineage indicated by alpha-smooth muscle actin (SMA) and brachyury positive
1070 cells after 4 DIV. Scale, 10 μ m. **d**, Comparison of the anti-MMUT (green) staining pattern
1071 from representative patient fibroblast-derived iPSCs compared to controls. Representative
1072 images come from cell line Ct1.2 and Pt1.1 For reference, anti-TOMM20, a mitochondrial
1073 protein, is also shown (red). Scale, 50 μ m. **e**, Western blotting analysis of derived iPSCs
1074 using anti-MMUT. MMUT is anticipated at 83 kDa. The loading control ACTB is anticipated
1075 at 42 kDa. Uncropped membranes are available in Supp. Fig. 12. **f**, Propionate incorporation
1076 of two Ct1.1 and Ct1.2 wildtype iPSC sub-clones and Pt1 and Pt2 patient cell lines. Data
1077 points represent independent measurements taken from 3 separate cultures per cell line.
1078 Mean control iPSC incorporation values were 22.71 and 24.36 pmol/mg.protein/16h. Patient
1079 iPSC incorporation values were 0.77 pmol/mg.protein/16h in Pt1 and 0.44
1080 pmol/mg.protein/16h in Pt2. P-value was tested using Mann-Whitney U-test (**, <0.01). Error
1081 is presented as standard deviation.

1082
1083 Figure Caption, Main figure 2:
1084 **Derivation of cortical neurons from iPSCs affected by methylmalonic aciduria.** **a**,
1085 Schematic of the 2D neuron differentiation protocol used in this article. Created using
1086 BioRender Forny, P. (2025) <https://BioRender.com/w70y299>. **b**, Staining for SSEA4 and
1087 SOX2 at day 0 for pluripotent stem cells (iPSC). Staining for Nestin (NES) and SOX2 at day
1088 13 for neuroepithelium. Staining for PAX6 and SOX2 at day 21 for neural stem cells (NSCs).
1089 Staining for TUBB3 and EOMES at day 40 for cortical progenitors. Staining for TUBB3/TBR1
1090 and MAP2/NeuN at day 50 signal postmitotic deep layer cortical neurons and pan-neuronal
1091 molecular markers in cultures, respectively. Scale: iPSCs and neurons have 10 μ m bars.
1092 Neuroepithelium, NSC, and NPCs have 50 μ m bars. **c**, RT-qPCR of SOX2, PAX6, and
1093 EOMES in iPSCs at day 0, neuroepithelium day 13, and NSCs day 21. Datapoints are
1094 representative of at least 3 independent experiments and error is reported as standard
1095 deviation. Expression values are relative to measurements at day 0 for each cell line. **d**,
1096 Immunocytochemistry of patient and control NSC and neurons. Scale, 10 μ m. **e**, Western
1097 blotting analysis of neurons using anti-MMUT. MMUT is anticipated at 83 kDa. The loading
1098 control ACTB is anticipated at 42 kDa. Uncropped membranes are available in Supp. Fig.
1099 12.

1100
1101 Figure Caption, Main figure 3:
1102 **Patient neurons show mitochondrial dysfunction that overlaps with loss of MMUT**
1103 **protein** **a**, Left and middle: MMUT+ signal (green) and TOMM20+ mitochondrial signal (red).
1104 Right: TOMM20+ signal (magenta) and colocalization with MMUT (white). Representative
1105 images were selected from Ct1.2 and Pt1.2 cell lines. Orthogonal representative slices are
1106 also shown. Scale is 10 μ m. **b**, Pearson correlation coefficient of TOMM20+ regions of
1107 interest (ROIs). One data point represents a Pearson's coefficient from one ROI. 3-5 ROIs
1108 per image, total images used from control $n = 6$ (18 total ROIs) and from patient $n = 11$ (50
1109 total ROIs). P-value determined by one-way ANOVA with multiple testing (ns, >0.05; ****,
1110 <0.0001) Datapoints represent Ct1.2, Ct2, Pt1.1, Pt1.2, and Pt2.1. Error is plotted as min. to
1111 max. **c**, Neuronal mitochondria stained with MMUT and TMRM (both grey). Scale is 10 μ m.
1112 Representative images were selected from Ct2, Pt1.1, and Pt2.1 **d**, TMRM+ ROIs selected
1113 from non-overlapping confocal images. Cumulative data is representative of $n = 6$ in control
1114 without rotenone, $n = 4$ in control with rotenone, $n = 8$ in patient without rotenone, $n = 9$ in
1115 patient with rotenone. One datapoint represents one background/size-corrected ROI. P-

1116 value determined by Kruskal-Wallis with multiple testing (ns, >0.05 ; *, <0.05 ; ****, <0.0001).
1117 Datapoints represent Ct2, Pt1.1, and Pt2.1. Bar represents the median value. **e**, Western
1118 blotting analysis of MMUT, caspase-3 (CASP3), its cleaved product, and β -actin (ACTB) in
1119 total cell lysate from untreated neurons. Each column represents an independent lysate.
1120 Uncropped membranes are available in Supp. Fig. 12. **f**, Quantification of DAPI+ apoptotic
1121 cells determined from representative, non-overlapping, epifluorescent images acquired using
1122 a 63x objective. Images were taken of fixed untreated neurons at day 50 *in vitro*. Datapoints
1123 in control represent Ct1.2 and Ct2, and datapoint in patient represent Pt1.1, Pt1.2, Pt2.1,
1124 and Pt2.2. Cumulative data is representative of $n=43$ (776 cells) in control and $n=87$ (1317
1125 cells) in patient images. Significance is assessed by Mann-Whitney test (****, <0.0001).
1126 Error is standard deviation. Dunn's multiple comparisons test used in b, d.
1127

1128 Figure Caption, Main figure 4:

1129 **Patient neurons show action potential exhaustion driven by reduced sodium currents.**
1130 **a**, First two dimensions (44% variance explained) of a principal component analysis of 21
1131 measured features from patient ($n=132$ (Pt1 $n=77$, Pt2 $n=55$)) and control ($n=94$ (Ct1
1132 $n=59$, Ct2 $n=35$)) neurons. Greyscale represents 3 identified neuronal types, type 1 (light
1133 grey, T1, $n=60$), type 2 (dark grey, T2, $n=64$), and type 3 (black, T3, $n=102$). **b**, Current-
1134 clamp, representative traces from T1, T2, or T3 neurons in response to depolarizing current
1135 injection. **c**, Proportional generation of classified neurons of control (Ct1, Ct2) and patient
1136 (Pt1, Pt2). **d**, Correlation matrix of 21 features in patient (bottom-left, orange) and control
1137 (top-right, blue) neurons. Positive correlations indicated by red and negative by blue.
1138 Features with significance $P= <0.01$ are displayed on the matrix, values above are blank. **e**,
1139 Top, overlayed traces from T3 control and patient neurons. Bottom, attenuation ratio from
1140 102 measured T3 neurons. **f**, Phase plots of 2 overlayd single action potentials from
1141 representative T3 control and patient neurons. **g**, Depolarisation (left, maximum dV/dt) and
1142 repolarisation (right, minimum dV/dt) velocities. **h**, Voltage-clamp, representative overlay of
1143 currents evoked by step to -30 or -20 mV in control and patient neurons, respectively. Inset
1144 is an enlarged section of the initial segment. **i**, Peak control ($n=67$) and patient ($n=66$)
1145 sodium current densities. **j**, Peak and steady control ($n=67$) and patient ($n=66$) potassium
1146 current densities. In i-j, current densities are normalised to capacitance, and variation is SD
1147 and present as shaded area. In e and g, datapoints represent one neuron, data are pooled
1148 into control (2 independent lines) and patient (2 independent lines), significance is by t-test
1149 and reported with p-value adjustment using Holm, and whiskers represent 1.5·IQR.
1150

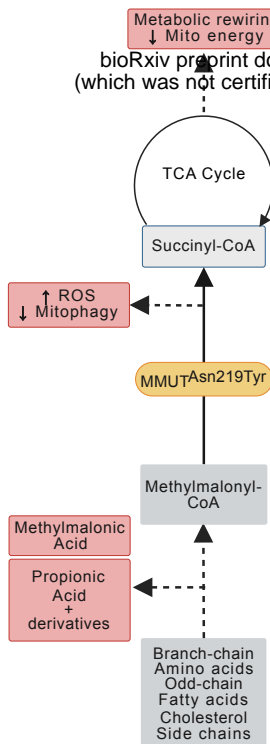
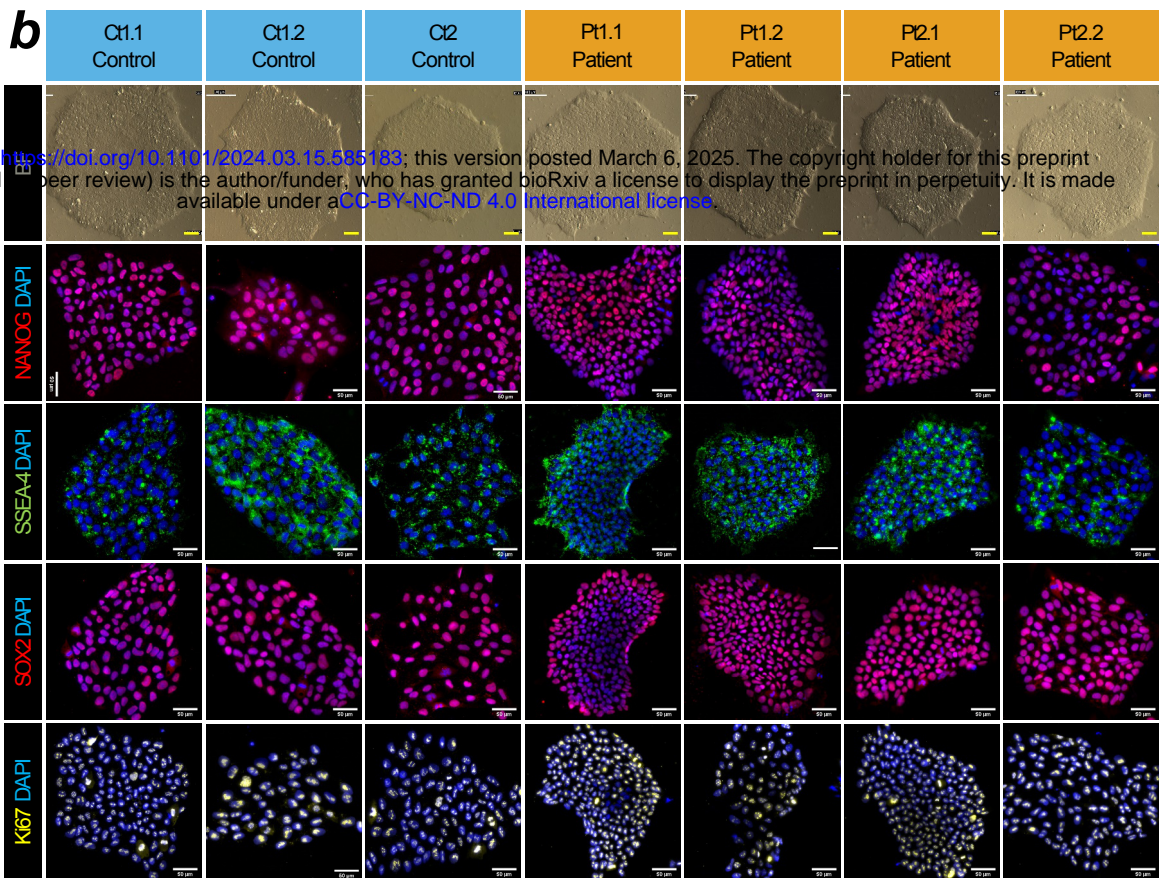
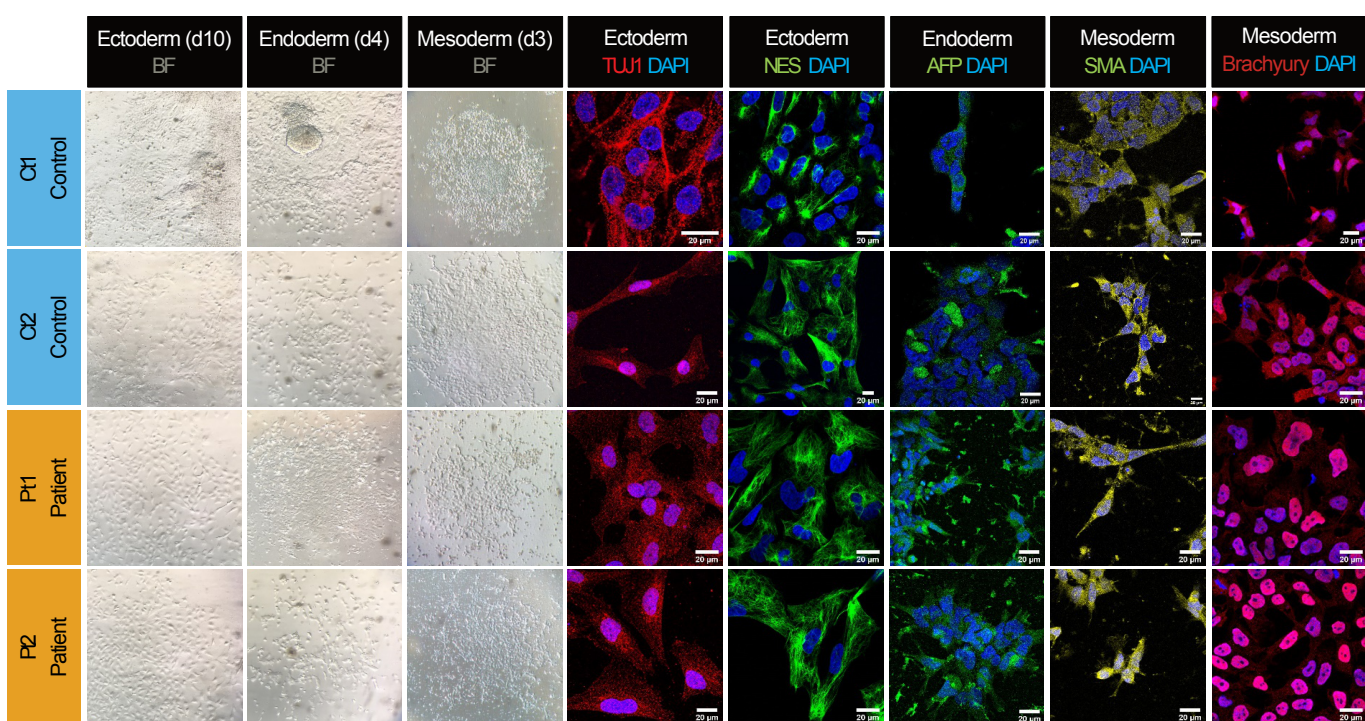
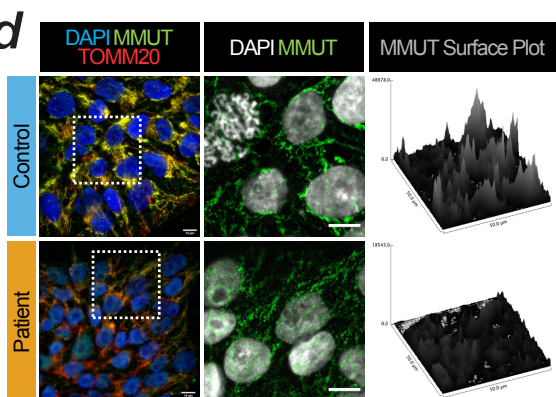
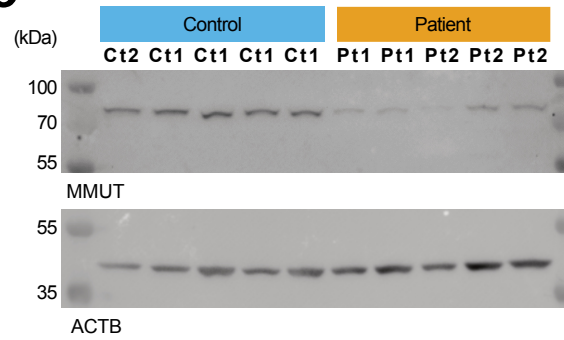
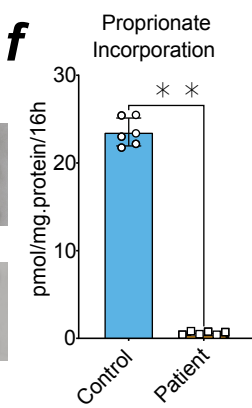
1151 Figure Caption, Main figure 5:

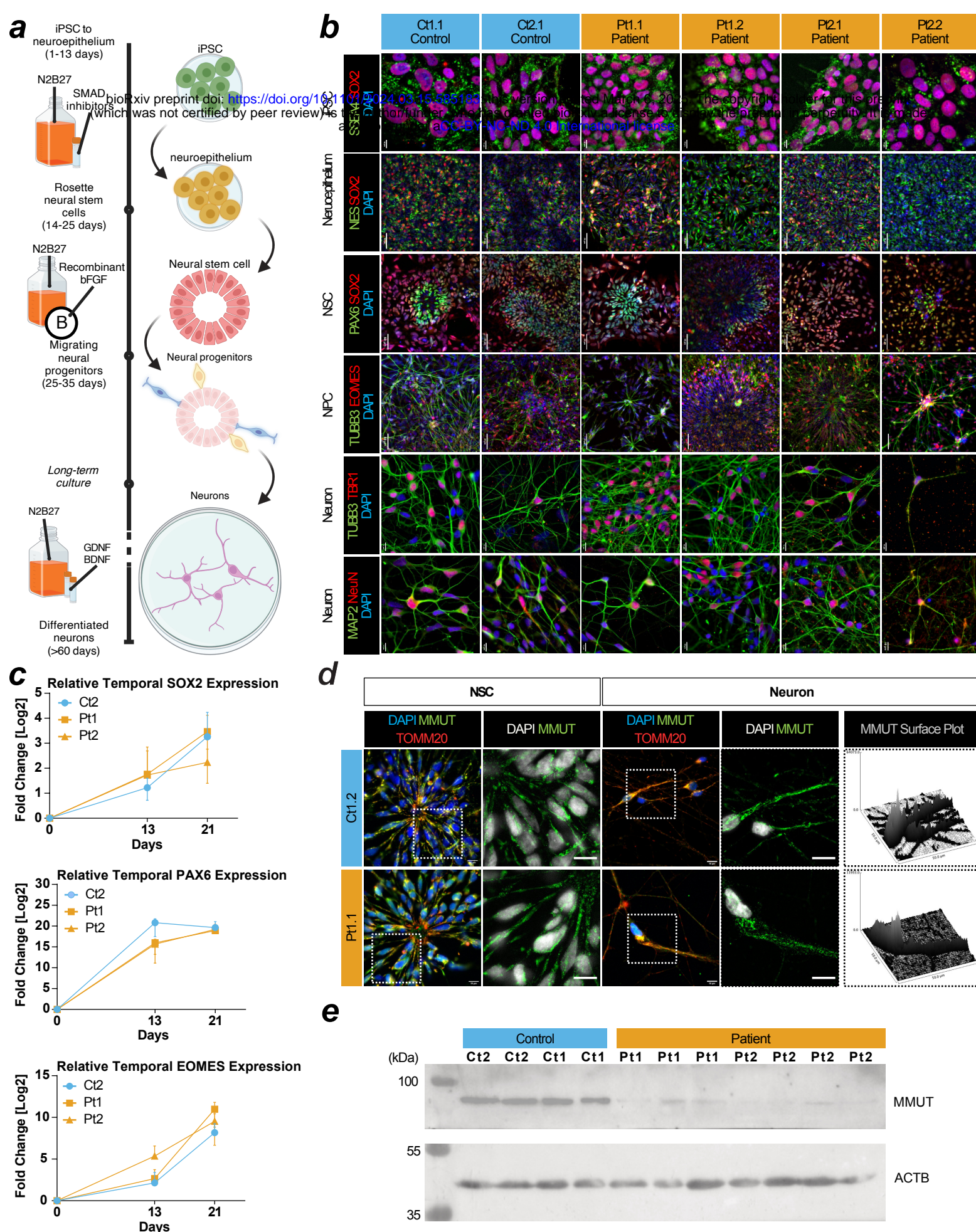
1152 **Metabolomics reveal dysregulated glutamate and glutamine neuronal metabolism.** **a**,
1153 Box plots of absolute ion abundance of disease-related metabolites. P-value is reported as
1154 one-way ANOVA for hydroxypropionic acid, and unpaired t-test for propionyl-carnitine, and
1155 lactate. **b**, Schematic of labelled ^{13}C -glutamine metabolism into the TCA cycle. Labelled
1156 carbons = filled black circles. **c** Stacked bar chart of contribution of labelled glutamine
1157 carbons to aspartate (left) and box plot of absolute ion abundance of aspartate pool (right).
1158 P-value calculated via unpaired t-test. **d**, Box plot of ratio between M+5 to M+4 labelled
1159 citrate fractions (left) and box plot of ratio between M+3 to M+4 labelled malate or aspartate
1160 fractions (right). P-value is reported as unpaired t test. **e**, Representative schematic for the
1161 entry of dimethyl-2-oxoglutarate (DM-2OG) into the TCA cycle and selected anaplerotic
1162 entry points. **f**, Box plot of absolute ion abundance of propionyl-carnitine and lactate in DM-
1163 2OG treated neurons. P value is reported as unpaired t test. **g**, Box plot of total fractional
1164 contribution of carbons to untreated and DM-2OG treated neuronal abundance of aspartate.
1165 P-value is reported as Mann-Whitney (left). **h**, Stacked bar chart of contribution of labelled
1166 carbons to untreated and DM-2OG treated neuronal abundance of malate (left) and citrate
1167 (right). **i**, Box plots of ratio between M+3 to M+4 labelled aspartate and malate fractions (left
1168 and right) in DM-2OG treated neurons and box plot of ratio between M+5 to M+4 labelled
1169 citrate fractions (middle) in DM-2OG treated neurons. In **a**, **c**, **d**, **f**, **g**, **h**, error = min/max (box
1170 plot) or SD (fractional bar plot). Each datapoint represents 3 technical replicates from one

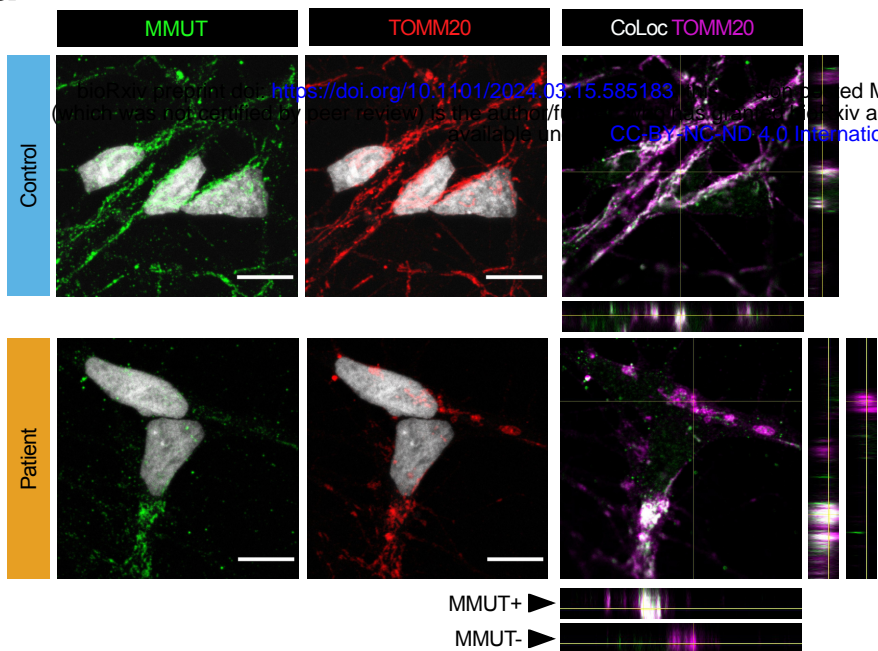
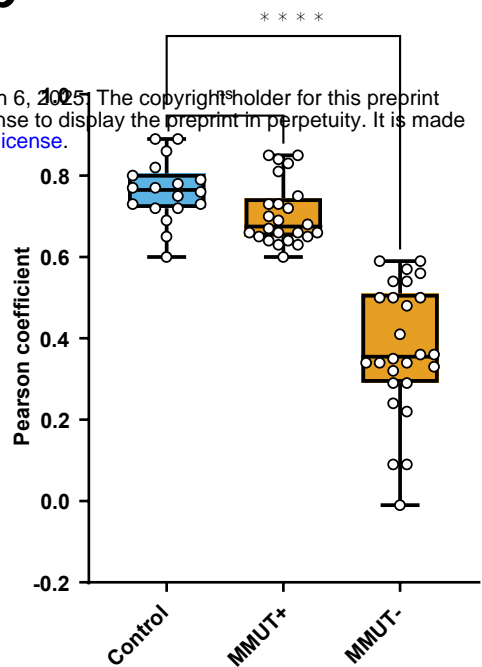
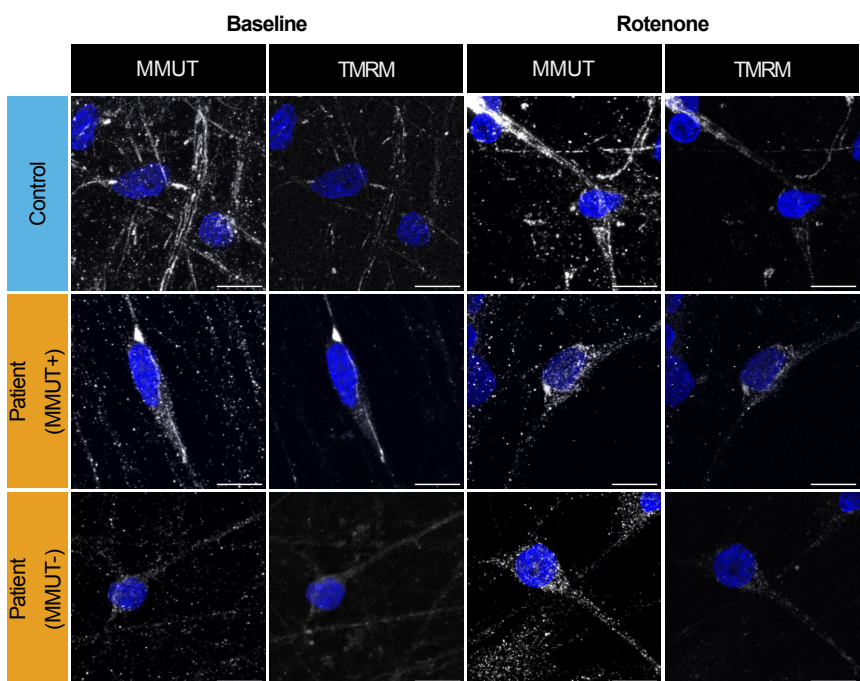
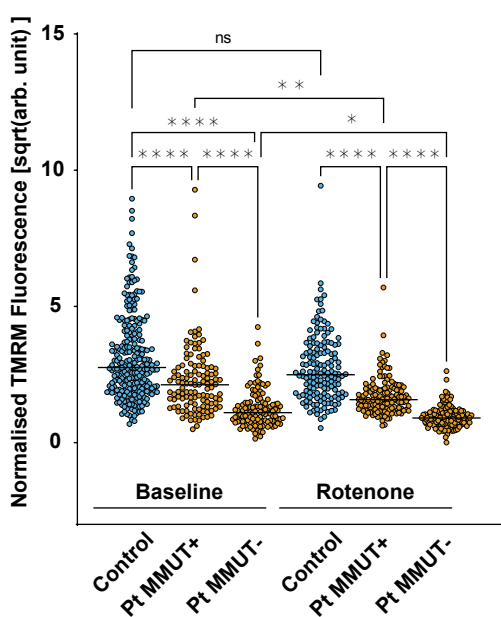
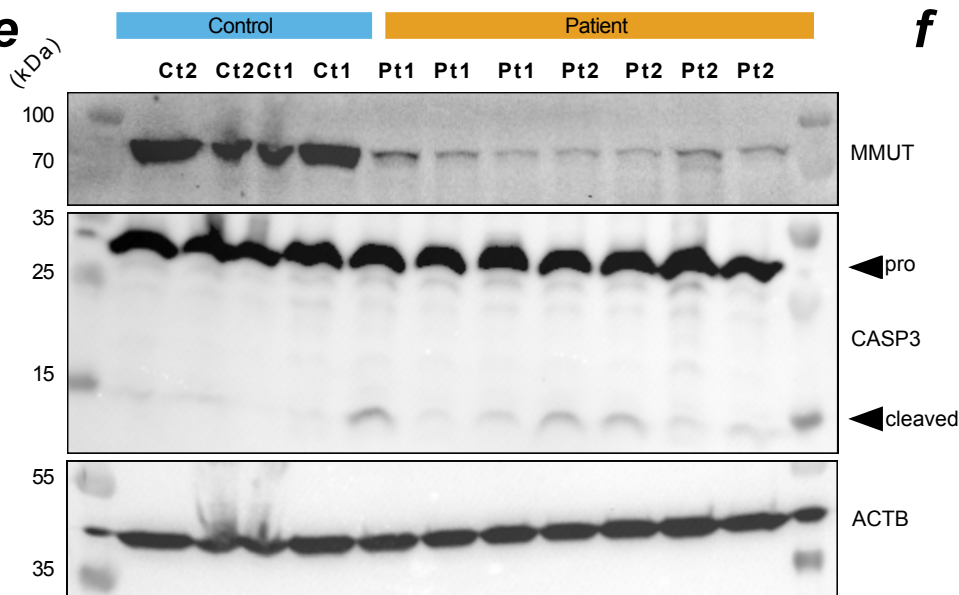
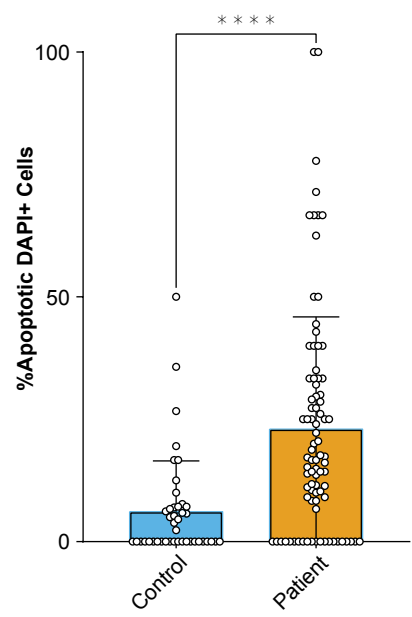
1171 independent sample. Genotype conditions are pooled into control (blue) and patient (no
1172 colour). In significance tests: ns = >0.05 , * = <0.05 , *** = <0.001 , **** = <0.0001 . In all
1173 panels, control is represented by Ct1.2 and Ct2. Patient is represented by Pt1.2 and Pt2.2.
1174

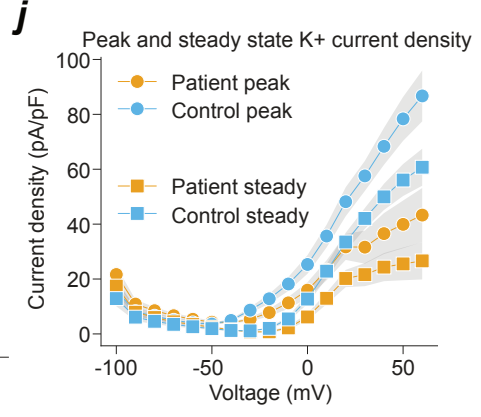
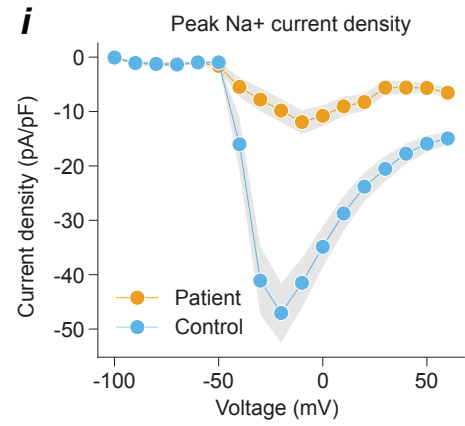
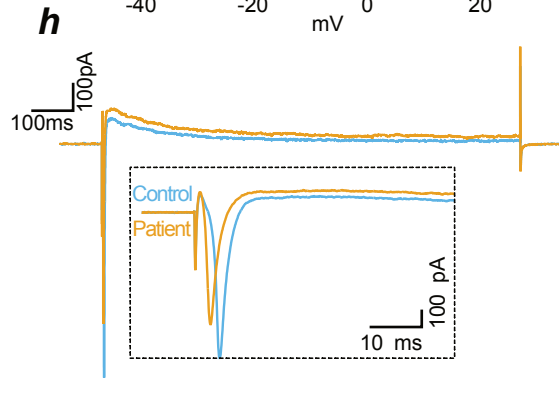
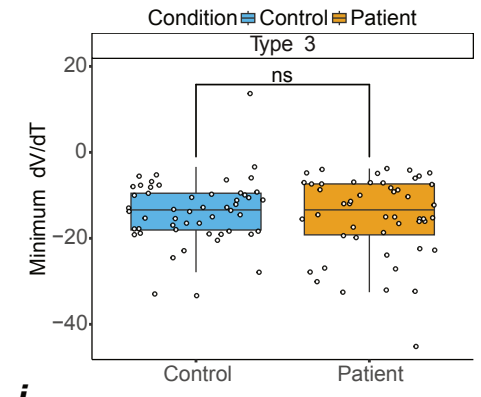
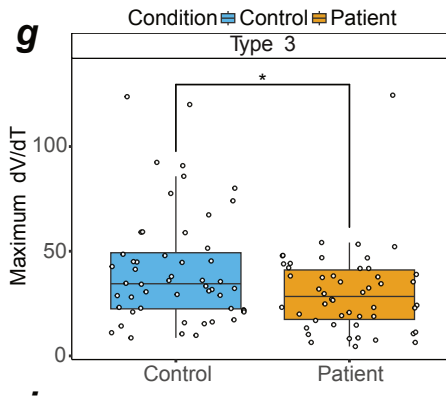
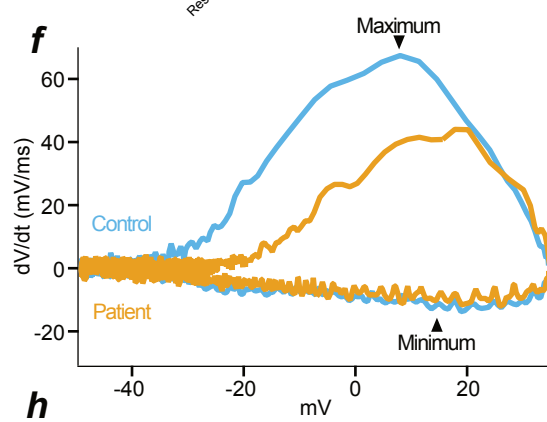
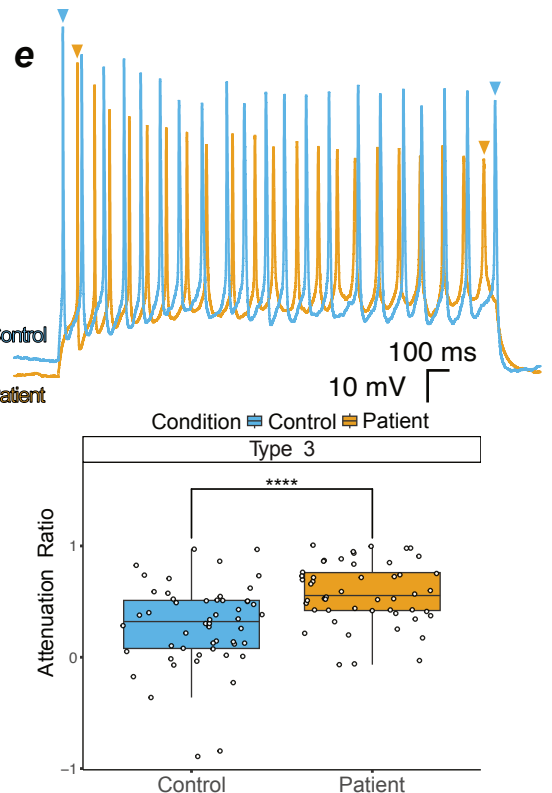
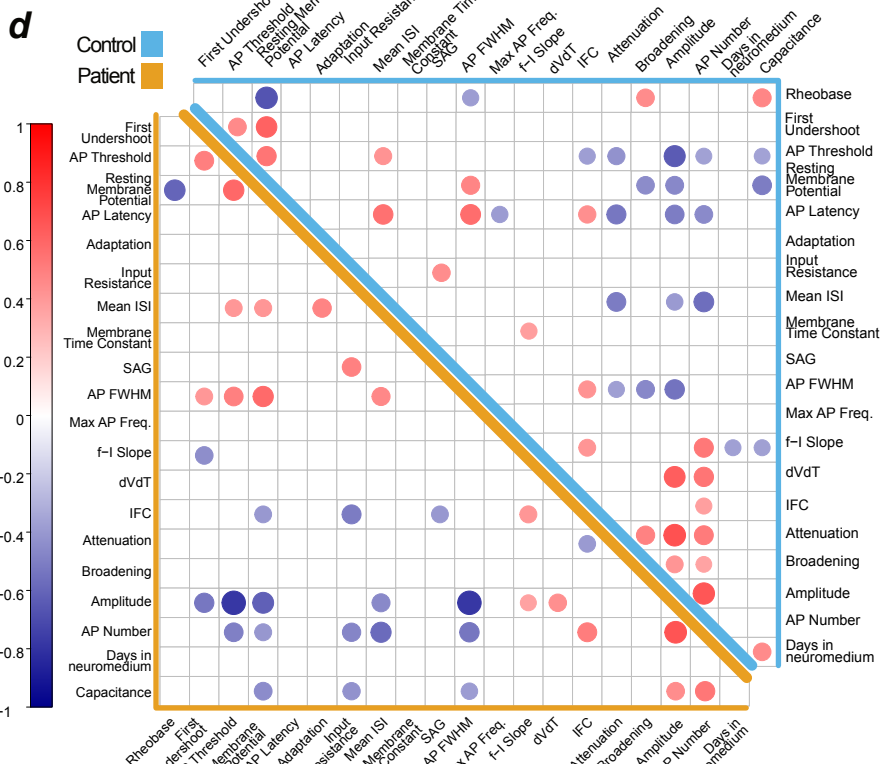
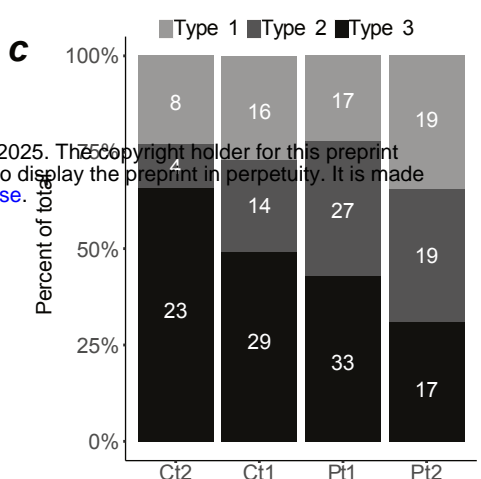
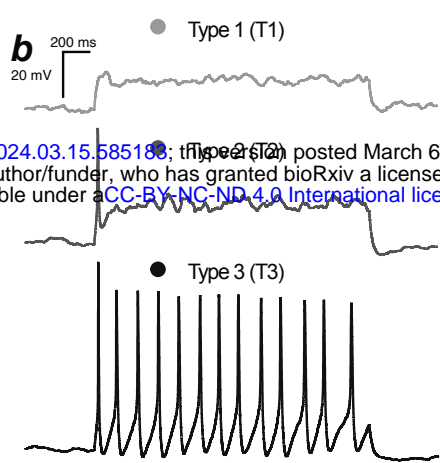
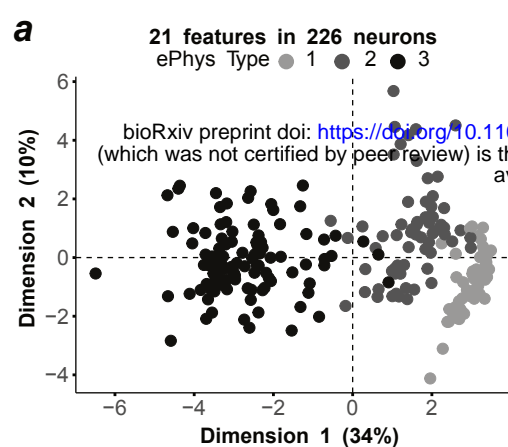
1175 Figure Caption, Main figure 6:

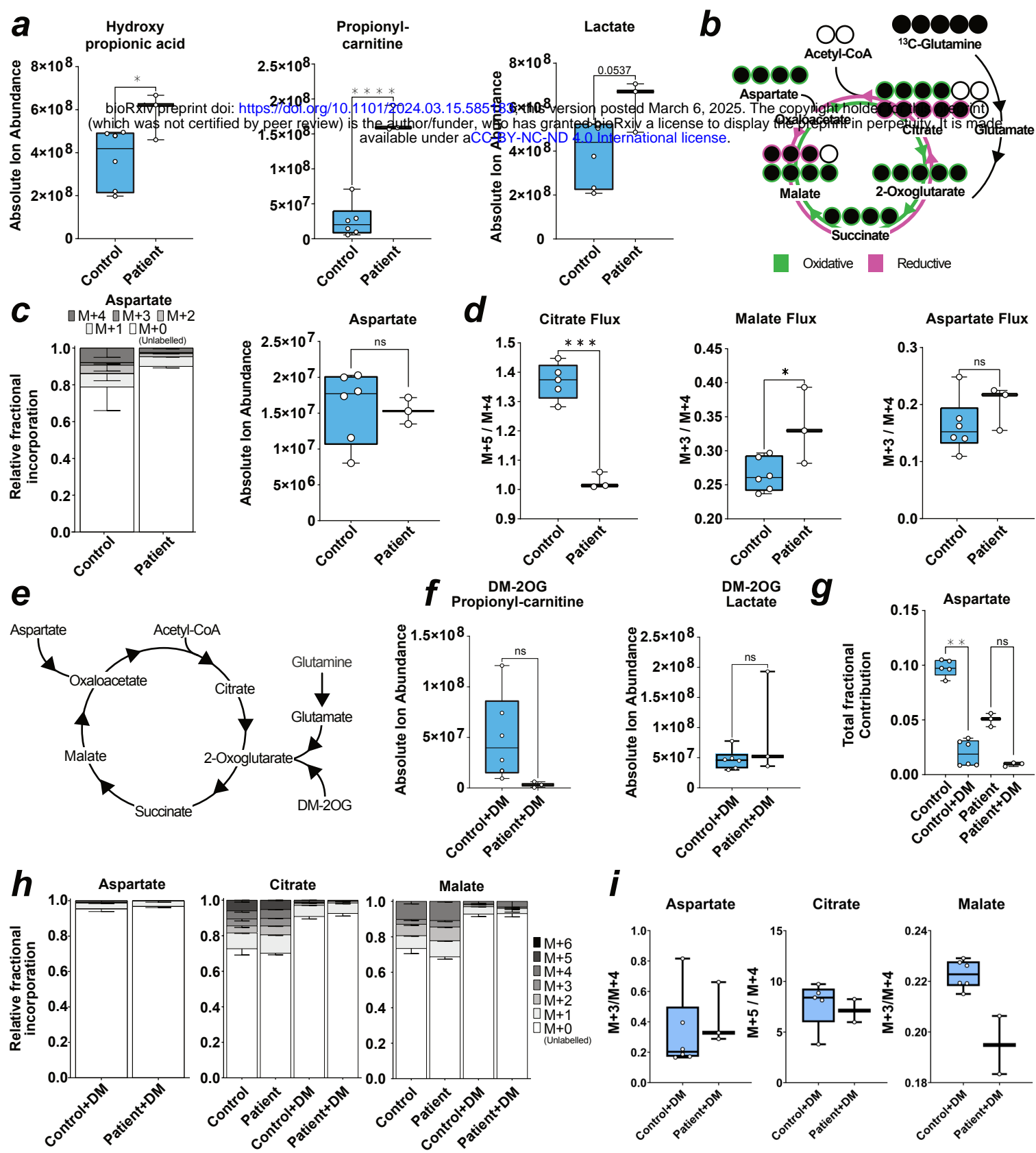
1176 **Metabolic rewiring affects glutamatergic synaptic transmission** **a**, Line graph indicating
1177 maximum current density at evoked voltages in control neurons with various DM-2OG
1178 treatments. Datapoint represents at least 5 independent samples, error = SD represented by
1179 shading. **b**, Line graph indicating maximum current density at evoked voltages in patient
1180 neurons with various DM-2OG treatments. Datapoint represents at least 6 independent
1181 samples, error = SD represented by shading. **c**, Representative averaged traces of
1182 spontaneous synaptic currents from single control (n events = 114) or patient (n events = 36)
1183 neurons in voltage-clamp. **d**, Box plot of spontaneous synaptic event charge of individual
1184 neurons in voltage-clamp. *P* value is calculated via mann-whitney **e**, Over-representation
1185 analysis of top 10 up and down-regulated GO terms from untreated control (*n* = 5) and
1186 patient (*n* = 6) derived neurons. Count refers to number of contributing genes. **f**, Volcano plot
1187 of differential regulation between untreated control (*n* = 5) and patient (*n* = 6) neurons. **g**,
1188 Over-representation analysis of top 10 up- and down-regulated GO terms. Count refers to
1189 number of contributing genes from untreated control (*n* = 5) and 0.1 mM DM-2OG treated
1190 patient (*n* = 4) derived neurons. **h**, Volcano plot of differential regulation between untreated
1191 control (*n* = 5) and 0.1mM DM-2OG treated patient (*n* = 4) neurons. In **c**, **d**, each datapoint
1192 represents one independent sample. Genotypes are control (blue) and patient (orange). In **a**,
1193 **b** center is the mean and error are SD. In **c**, **e**, colour represents *P* value magnitude. In **f**, **h**,
1194 values are FDR, genes highlighted contribute to a top differentially regulated GO term.
1195 Dotted lines indicate Log2 fold change of 1 and -log10 *P*-value of 0.01. In **d**, box plot is
1196 median and min/max. In panels a-d, control is represented by Ct1 and Ct2, and patient is
1197 represented by Pt1 and Pt2. In panels e-h, control is represented by Ct1.2 and Ct2, and
1198 patient is represented by Pt1.1, Pt1.2, Pt2.1, and Pt2.2.
1199

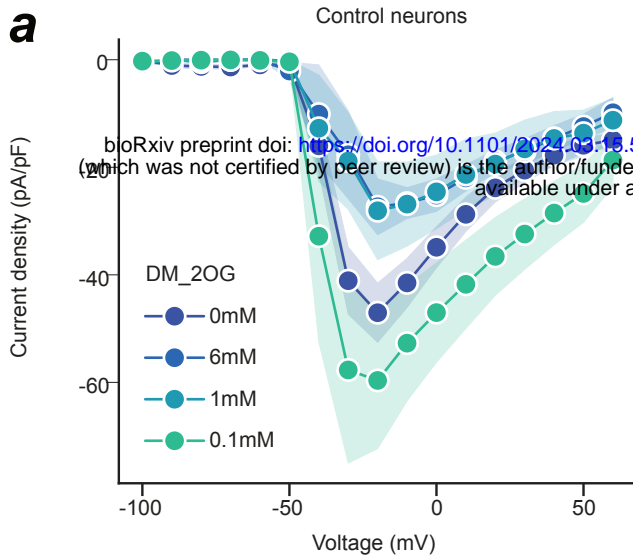
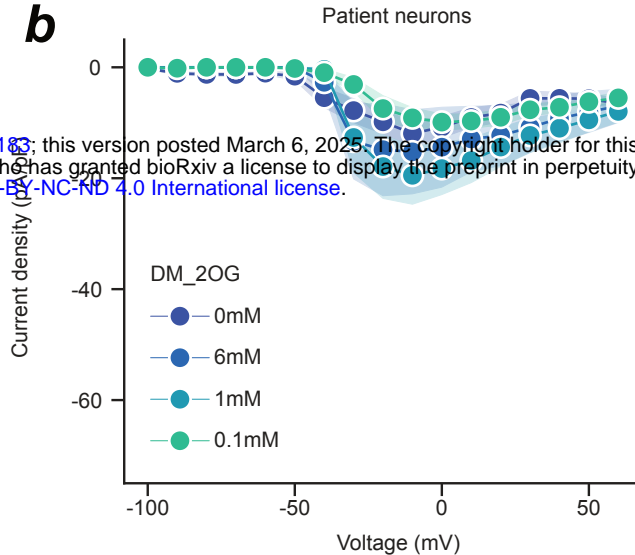
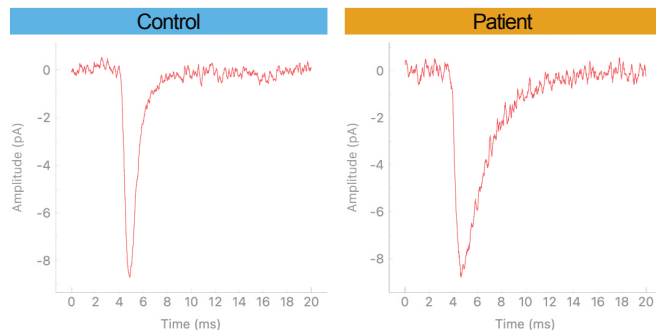
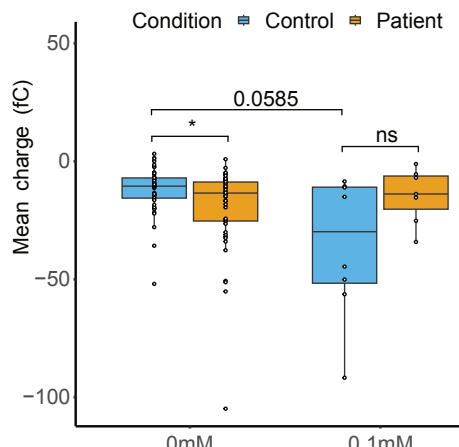
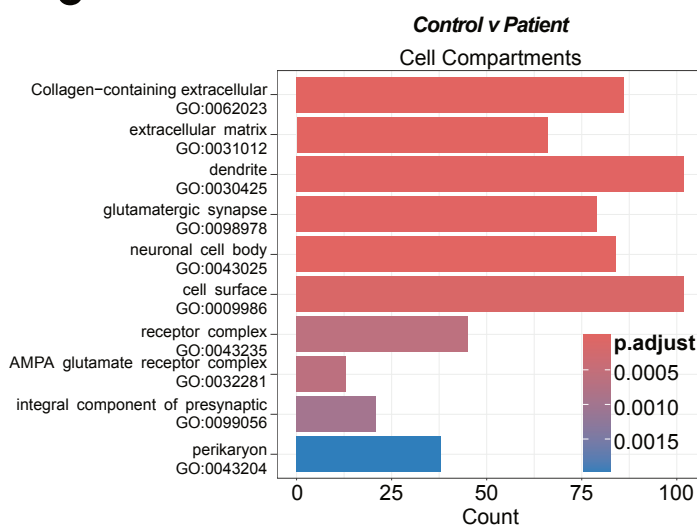
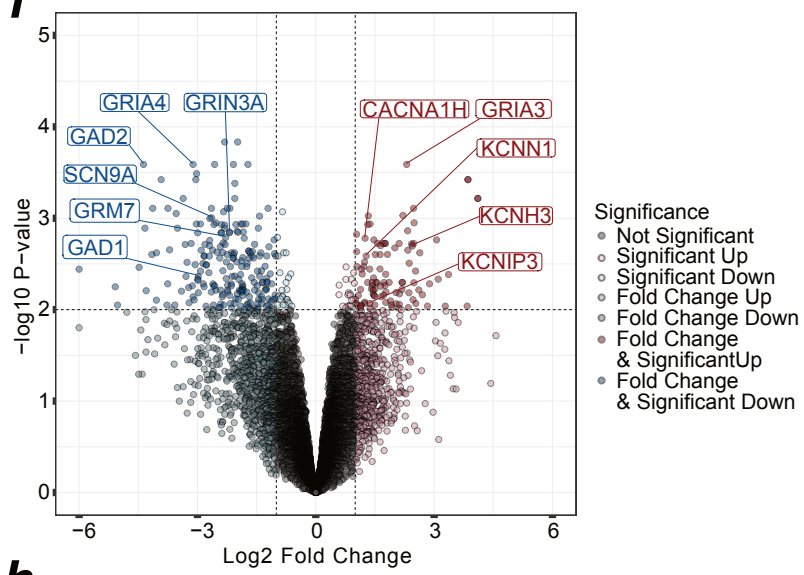
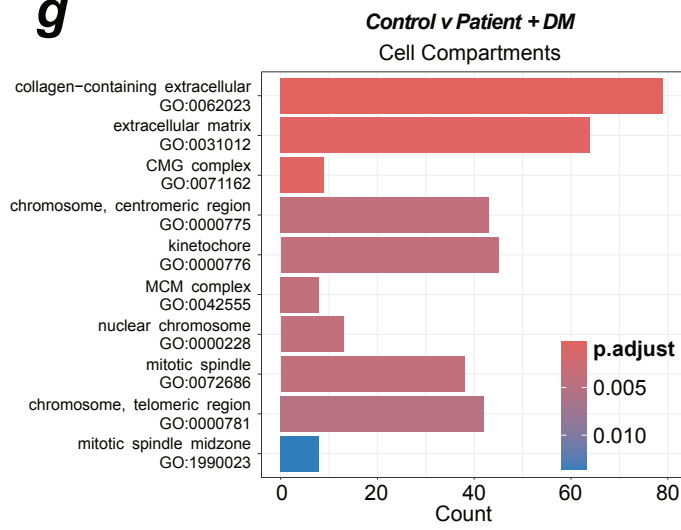
a**b****c****d****e****f**



a**b****c****d****e****f**





a**b****c****d****e****f****g****h**